Spectral Classification of Neutron Star Post-Merger Gravitational Wave Emission

Author: Ioannis Koutalios
Supervisor: Nikolaos Stergioulas

Department of Astrophysics, Astronomy and Mechanics
Department of Physics
Aristotle University of Thessaloniki

October 13, 2020

Abstract

The post-merger phase of binary neutron star mergers includes the imprint of distinct gravitational-wave emission processes. We compute Fourier spectra for a large number gravitational wave signals that were produced through simulations and were made available by three different numerical relativity groups and find they are well described by the classification proposed in Bauswein and Stergioulas (2015). For all cases, we also compute time-frequency spectrograms to distinguish the early from the late emission. In addition, we reproduce some empirical relations that were recently proposed and connect the properties of the neutron stars in the inspiral phase to the main frequency peak in the post-merger phase.

Acknowledgements

I would like to express my deep gratitude to my supervisor, professor Nikolaos Stergioulas. His guidance and trust made this project possible and also gave me the confidence to make my first steps into the world of scientific research. My family has supported me all these years, from my mother always being there for me, to my father giving me endless physics lessons, their contribution to who I am can not be overstated. My friends also played a crucial role, by allowing me to be myself around them, and make interesting conversations. I want to thank them with all my heart. Shutout to all the members of the Gravitational Waves Team of A.U.TH. and especially to S. Vretinaris and G. Lioutas for helping me during this process.

I would like to dedicate this thesis to professor John H. Seiradakis. He was there for my baby steps into the world of astronomy and astrophysics and his belief in me, guidance and support gave me the confidence to become better. He will always be remembered.

Contents

Chapter 1

Introduction

We provide some very general information about neutron stars (NS) and and gravitational waves (GW) following the review articles and textbooks [1–6].

1.1 Neutron Stars

Neutron stars are formed from massive stars, heavier than about eight times the mass of our sun, but not heavier than about 20 times. They are the product of the core collapse of those stars, which tis accompanied by a supernova explosion. A prime example of such an explosion is the Crab Nebula, which hosts a neutron star at its center and is the remnant of a supergiant star that exploded at 1054. When the core of the star becomes iron rich, it can no longer produce energy by nuclear fusion, because iron 56 has the highest binding energy, and is thus not favorable to be fused into heavier elements. This leads to a point at which the electron degeneracy pressure, which supports a star against gravitational collapse, is no longer able to complete this task, allowing the core to collapse and form a neutron star, while the other outer layers of the star bounce off, leading to the explosion that is observed as a supernova.

At high densities, protons and electrons are combined in order to form neutrons plus neutrinos. During this process neutrinos escape, creating a neutrino burst. The neutrons settle down and create a neutron star, with the neutron degeneracy as the main force opposing a total gravitational collapse. The first discovery of a neutron star came from Jocelyn Bell in 1968 [7], with the observation of a pulsar, which is a fast rotating, magnetized neutron star. With more research and observations, it became clear that neutron degeneracy could not be the only force holding a heavy neutron star star from becoming a black hole, and that repulsive nuclear forces also had to play a role in supporting these structures. The mass range of neutron stars is currently estimated to be $1.0-2.5M_{\odot}$ with the upper limit still being very uncertain. At the moment, the uncertainty in the radius is also large and a typical neutron star could have a radius of 11 km or of 14 km.

There are many question that remain to be answered andsome of them will hopefully be solved by more detections of gravitational wave signals from binary neutron star mergers. Such questions are the composition of matter at the high densities that are present inside a neutron star, differences between normal and neutron-rich matter and the ability to calculate from first principles how matter behaves in β equilibrium. The motivation behind a better understanding of the

nature of neutron stars is not only to be able to describe them more accurately. Neutron stars serve as an important laboratory for discovering new physics and they are relevant to several other fields of physics, bringing together scientists and necessitating a collaboration between such fields in order to properly observe, explain and predict phenomena related to them. A breakthrough in our understanding of neutron stars can lead to a better and deeper understanding of nuclear and theoretical physics, as well as several other fields.

1.2 Gravitational Waves

Einstein explained gravity is the result of the curvature of spacetime. In the absence of mass, spacetime remains flat, but the presence of any mass or energy curves space and time. This idea led to the field equations of the General Relativity (GR). Any asymmetric (equal or higher than quadrupolar) changes in the position of masses leads to the creation of "ripples" in spacetime, meaning a wavelike change of the gravitational field. Much like how the motion of charged particles will create electromagnetic waves, moving masses create gravitational waves. Because gravity is $\sim 10^{40}$ times weaker than the electromagnetic force, such waves are not having any effects that can be observed without appropriate instruments. An example of a strong gravitational wave source are two black holes merging into one. Events like this are extremely rare in our universe. The effect that this will produce, here on Earth, is a displacement that will be almost 1000 times smaller than the diameter of a single proton.

Not every motion of mass will create gravitational waves. A perfectly shaped star, for example, spinning axisymmetrically around its own axis will not create gravitational waves. If the star has some anomalies on its surface, then gravitational waves will be produced depending on the degree of its asymmetry. Another example is supernova explosions. If we assume that the explosion is spherically symmetric, there should be no gravitational waves emitted. However our understanding of such explosions is that it is not perfect and the ejection is far from being symmetric, so we anticipate that gravitational waves are being produced and that we will one day be able to detect them.

So far, the only sources of gravitational waves that have been observed with our current technology are waves being produced during the late stages of binary systems. The so called inspiral gravitational waves are generated during those events, where two compact binary objects such as black holes and/or neutron stars are merging into one. Such systems are constantly producing gravitational waves, which leads to an energy loss, allowing the system to come closer and closer. Near the point of coalescence, the two objects are emitting gravitational waves strong enough to be detected with our equipment. The frequency is rapidly increasing, producing a characteristic "chirp sound".

The first pair of neutron stars was observed by Hulse and Taylor in 1974 [8]. The system consists of a pulsar in orbit with another neutron star. The decay of the orbit of the system was matched exactly with the predictions of general relativity, providing us very strong, although not direct, evidence that gravitational waves, as predicted by Einstein's general relativity, do exist. The discovery of PSR B1913+16 (the name of the binary system), as well as the measurements of the decay, gave Hulse and Taylor the Nobel Prize in 1993.

1.3 Detecting Gravitational Waves

The interaction of gravitational waves with matter leads to the compression of objects in one direction while stretching them in the perpendicular direction. One can imagine this by a square (e.g. 1m in length) which will be stretched and become a rectangle (e.g. 0.8m in length and 1.2m in width). Therefore, it makes sense to use L-shaped detectors and measure how the relative lengths of the two arms are changing, using interferometry. With interferometry we can observe patterns produced when two light sources are combined, so-called interference patterns. We can then know how the length of one arm is changing with respect to the other. Two such interferometers were build in the US, one in Hanford, Washington and the other in Livingston, Louisiana. They are called Laser Interferometer Gravitational-wave Observatory (LIGO) [9, 10]. There are more detectors scattered around the globe, VIRGO in Italy [11, 12], GEO600 in Germany [13, 14] and TAMA in Japan [15, 16].

There is a need for multiple interferometers in order to be able to detect gravitational waves. Using multiple detectors has the advantage of being able to locate the source, since a single directional detector cannot give us accurate sky localization. The finite speed of these waves (equal to the speed of light) means that there will be a delay between the detection at the first interferometer and the others and one can use the differences in orientation between the different detectors to infer the location of the source on the sky. This is one of the reasons why having multiple detectors is necessary, other than reducing the errors. Noise is something tricky for such detections, because as discussed previously, the displacements that one tries to measure are extremely small. Various sources, even tiny earthquakes can create signals that mimic gravitational waves, so analyzing the data of multiple detectors can cross out these local noises.

Gravitational wave antennas are essentially omni-directional, with linearly polarized quadrupolar antenna patterns that typically have a response better than 50% of its average over 75% of the sky. Their nearly all-sky sensitivity is an important difference from pointed astronomical antennas and telescopes. Gravitational wave antennas operate as a network, with the aim of taking data continuously. Gravitational wave detectors register gravitational waves coherently by following the phase of the wave and not just measuring its intensity. Since the phase is determined by large-scale motions of matter inside the sources, much of the astrophysical information is extracted from the phase. This leads to different kinds of data analysis methods than one normally encounters in astronomy, based on matched filtering and searches over large parameter spaces of potential signals. This style of data analysis requires the input of pre-calculated template signals, which means that gravitational wave detection depends more strongly than most other branches of astronomy on theoretical input. The better the input, the greater the range of the detectors.

The fact that detectors are omni-directional and detect coherently the phase of the incoming wave makes them in many ways more like microphones for sound than like conventional telescopes. The analogy with sound can be helpful, since microphones can be used to monitor environments for disturbances in any location, and since when we listen to sounds our brains do a form of matched filtering to allow us to interpret the sounds we want to understand against a background of noise. In a very real sense, gravitational wave detectors will be listening to the sounds of a restless universe. The gravitational wave "window" is actually a listening post, a

monitor for the most dramatic events that occur in the universe [5]

Chapter 2

EOS and Tidal Deformability

Of fundamental importance for neutron stars is the equation of state (EOS). The basis of this is to have equations describing the macrophysical quantities of the neutron stars, that we can observe, derived from the microphysical properties of matter. In order to do that we need an EOS in the form of $P(\epsilon)$, where P is pressure and ϵ is energy density and by using the GR equations with some symmetry assumptions we can derive a relation such as mass versus radius, $M(R)$. This problem was successfully solved by Tolman, Oppenheimer and Volkoff (TOV) [17], who independently solved this problem for static and spherically symmetric NS consisting of a perfect fluid.

2.1 The TOV set of equations

Using the metric for a spherically symmetric, stationary and asymptotically flat spacetime in Schwarzschild coordinates t, r, θ, ϕ

$$ds^2 = -e^{\nu}dt^2 + e^{\lambda}dr^2 + r^2(d\theta^2 + \sin^2\theta d\phi^2), \tag{2.1}$$

where $\nu(r)$ and $\lambda(r)$ are metric functions, the set of the TOV equations [17] can be written in the form:

$$P = P(\epsilon),$$

$$\frac{dP}{dr} = -\frac{(\epsilon + P)(m + 4\pi r^3 P)}{r(r - 2m)},$$

$$\frac{dm}{dr} = 4\pi r^2 \epsilon,$$

$$\frac{d\nu}{dr} = -\frac{2}{\epsilon + P}\frac{dP}{dr} = \frac{2(m + 4\pi r^3 P)}{r(r - 2m)},$$

$$\lambda = -\ln\left(1 - \frac{2m}{r}\right),$$

where $m(r)$ is the mass-energy contained within a sphere of radious r and we used $c = G = 1$. This set of differential equations is all we need in order to fully determine all the properties that we need for a neutron star, as long as the Someone needs to define the $P = P(\epsilon)$ relation is specified.

The EOS can be specified using several descriptions, such as :

- Microphysical (tabulated) EOS,
- Piecewise Polytropic approximation,
- Spectral approximation.

Throughout this thesis we will use the Piecewise Polytropic description, which will be described in detail.

2.1.1 Piecewise Polytropic description

We follow the work from [18]. A piecewise polytropic EOS is defined by a low-density $\rho < \rho_0$ part (which can be a tabulated crust EOS or its piecewise polytropic analytic approximation) and a high-density part, $\rho \geq \rho_0$. The matching baryonic (rest-mass) density ρ_0 is defined by the crossing point between the low-density part and the first high-density piece. The other two dividing densities in the high-density region are fixed as $\rho_1 = 10^{14.7}\mathrm{g/cm}^3$ and $\rho_2 = 10^{15.0}\mathrm{g/cm}^3$.

In this way, we create different intervals in which we have a different polytropic relation of the form

$$P = K_i \rho^{\Gamma_i}, \tag{2.2}$$

where K_i and Γ_i are the polytropic constant and the polytropic exponent, in each interval, respectively. The $P = P(\rho)$ relation has to be continuous for all the different densities. This means that at a dividing density ρ_i

$$P(\rho_i) = K_i \rho^{\Gamma_i} = K_{i+1} \rho^{\Gamma_{i+1}}.$$

For our three intervals we have an extra set of two equations reducing the free parameters from six to four. We define $K_1, \Gamma_1, \Gamma_2, \Gamma_3$ and derive the two remaining K_2, K_3.

In order to obtain the energy density, we need the first law of thermodynamics for barotropic fluids:

$$d\frac{\epsilon}{\rho} = -P d\frac{1}{\rho}. \tag{2.3}$$

Integrating for $\Gamma \neq 1$:

$$\epsilon(\rho) = (1 + \alpha_i)\rho + \frac{K_i}{\Gamma_i - 1}\rho^{\Gamma_i}, \tag{2.4}$$

where α_i is determined by requiring continuity in the energy density:

$$\alpha_i = \frac{\epsilon(\rho_{i-1})}{\rho_{i-1}} - 1 - \frac{K_i}{\Gamma_i - 1}\rho_{i-1}^{\Gamma_i - 1}. \tag{2.5}$$

We can now solve the TOV set of differential equations

$$\frac{d}{dr}\begin{bmatrix} P(r) \\ m(r) \\ \nu(r) \end{bmatrix} = \begin{bmatrix} -\frac{(\epsilon+P)(m+4\pi r^3 P)}{r(r-2m)} \\ 4\pi r^2 \epsilon \\ \frac{2(m+4\pi r^3 P)}{r(r-2m)} \end{bmatrix}, \tag{2.6}$$

just by defining $\{K_1, \Gamma_1, \Gamma_2, \Gamma_3\}$ or $\{p_1, \Gamma_2, \Gamma_3\}$ for the high-density part of the EOS (in addition to a chosen low-density part, which can also be represented in piecewise-polytropic form).

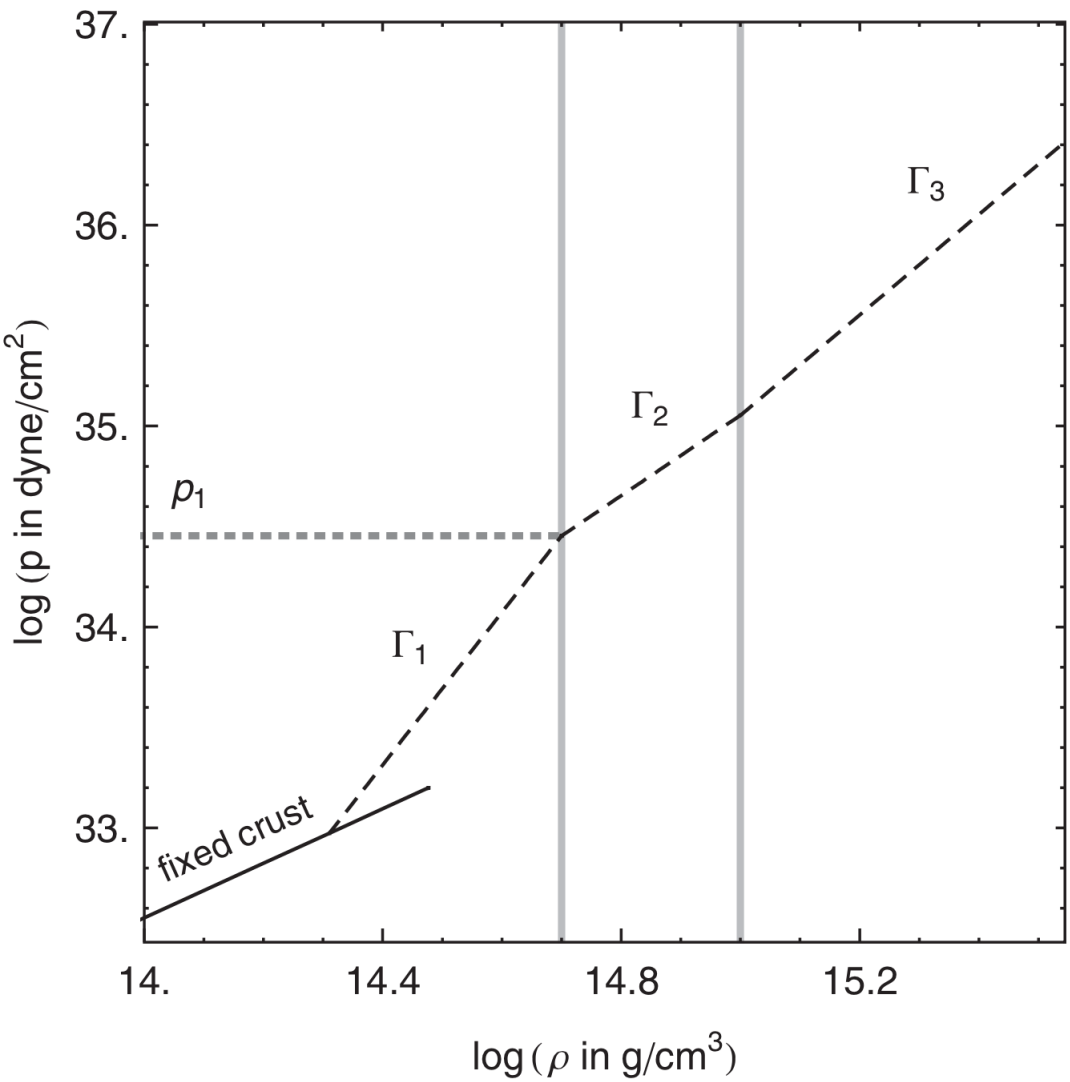

Figure 2.1: An example of a piecewise polytropic EOS. Te three intervals at high densities are shown match by a description of the crust. This relation has to be continuous at all densities. Figure from [19].

2.2 Tidal Deformability

The tidal deformability λ relating the star's induced quadrupole deformation Q_{ij} due to an external tidal field $\mathcal{E}_{ij}$ is defined through

$$Q_{ij} = -\lambda \mathcal{E}_{ij}. \tag{2.7}$$

The tidal deformability λ is related to the $l = 2$ dimensionless tidal Love number k_2 by:

$$k_2 = \frac{3}{2}\lambda R^{-5}, \tag{2.8}$$

and one can define the *dimensionless tidal deformability* as

$$\Lambda = \frac{\lambda}{M^5} = \frac{2}{3}k_2 \left(\frac{R}{M}\right)^5. \tag{2.9}$$

From Equation (2.7) and applying a linear $l = 2$ perturbation to a spherically symmetric neutron star, one can derive a second-order differential equation, which can then be simplified as a system of two first degree differential equations [20]

$$\frac{dH(r)}{dr} = \beta, \tag{2.10}$$

$$\begin{aligned}\frac{d\beta(r)}{dr} &= \frac{2rH}{r-2m}\left[-2\pi\left(5\epsilon+9P+\frac{\epsilon+P}{\frac{dp}{d\epsilon}}\right)+\frac{3}{r^2}\frac{2r}{r-2m}\left(\frac{m}{r^2}+4\pi rP\right)^2\right] \\ &+\frac{2\beta r}{r(r-2m)}\left[-1+\frac{m}{r}+2\pi r^2(\epsilon-P)\right],\end{aligned} \tag{2.11}$$

This set is added to the TOV equations and one can then calculate the tidal deformability by defining:

$$y = \frac{R\beta(R)}{H(R)}. \tag{2.12}$$

The $l = 2$ Love number is obtained as

$$\begin{aligned}k_2 = \frac{8C^5}{5}(1-2C)^2[2+2C(y-1)-y]\{2C[6-3y+3C(5y-8)]+ \\ +4C^3[13-11y+C(3y-2)+2C^2(1+y)]+3(1-2C)^2 \\ \times[2-y+2C(y-1)]\ln(1-2C)\}^{-1}.\end{aligned} \tag{2.13}$$

2.3 Equilibrium Models of Isolated NS

The integration of the previous set of five differential equations is performed numerically. We use the `pyTOVpp` code by N. Stergioulas [21] with some changes, that can be found here [22], in order to include the two equations for the tidal deformability. At first, someone has to define which EOS will be used, by fixing the low-density part of the EOS and choosing the high-density EOS through the choice of $\{p_1, \Gamma_2, \Gamma_3\}$.

For each equilibrium models, one defines the central density. Using a script that runs pyTOVpp in a loop for different central densities, the sequence of equilibrium models was obtained for each EOS, obtaining the relations $M = M(R)$, $k_2 = k_2(M)$ and $\lambda = \lambda(M)$. Results for a particular selection of EOS are shown in Figures 2.2 to 2.4 and agree with published results, see [23], [20], [24]

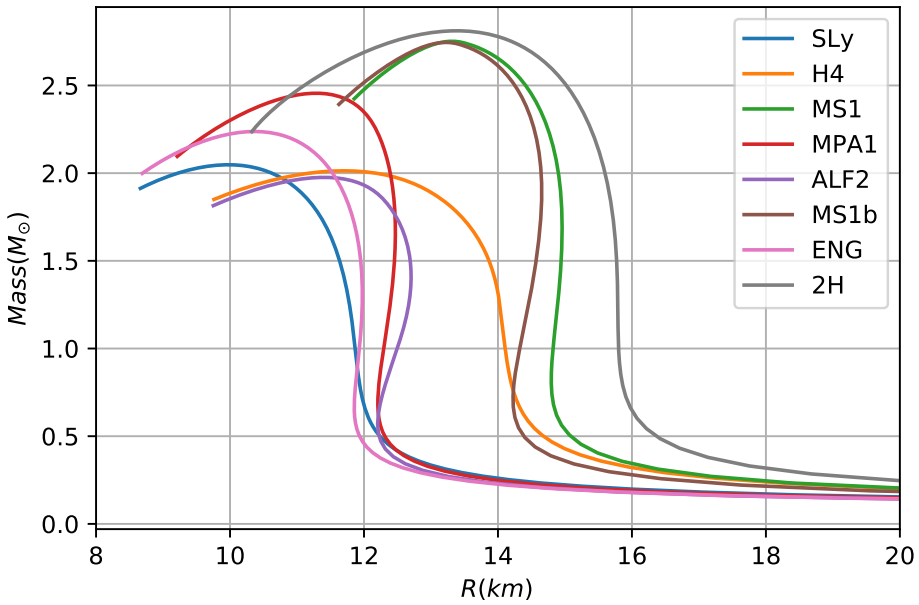

Figure 2.2: The mass vs. radius relation for different EOS as computed with the `pyTOVpp` code [21].

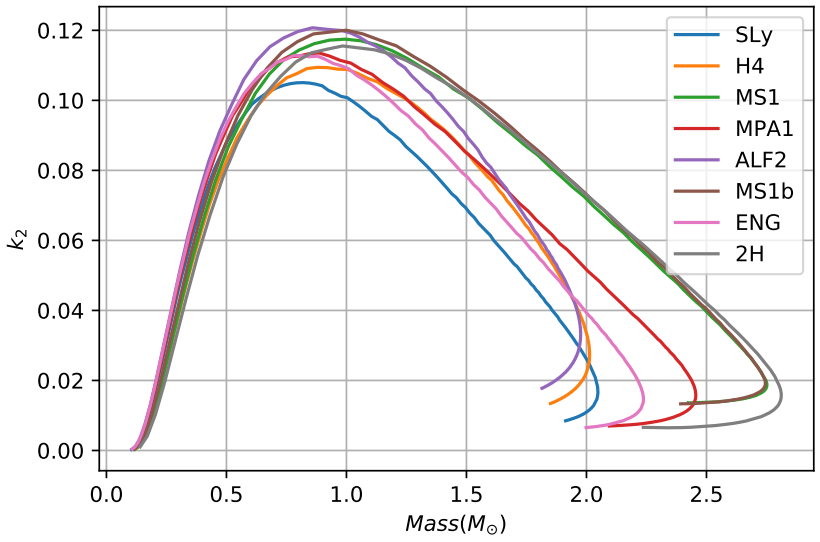

Figure 2.3: The Love number as a function of the mass for different EOS.

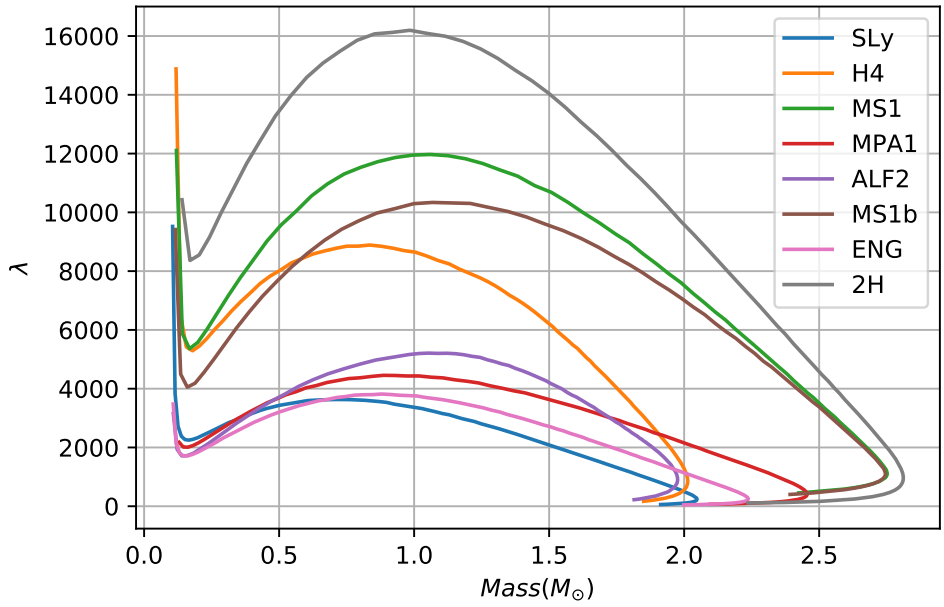

Figure 2.4: The dimensionless tidal deformability for various EOS.

Chapter 3

Empirical Relations in the Time and Frequency Domains

Some properties of merger remnant correlate well with the tidal deformability. We will use post-merger GW waveforms from the CoRe database [25] in order to confirm several empirical relations presented in [25].

3.1 Time Domain

The time difference between merger and the first post-merger minimum was shown in [25] to correlate with a mass-weighted tidal deformability. In addition, the amplitude of the first post-merger maximum was shown to have a specific dependence on the mass ratio of the binary. Figure 3.1 shows a representative GW waveform and three specific times that are of interest.

Here, the time of the merger is defined as the time of the GW peak amplitude. After that, the amplitude decreases as it reaches a lowest value, before increasing again for a few milliseconds, followed by a damping of oscillations in the post-merger phase. We are interested in calculating how the time $\Delta t_{\rm min}$ for the amplitude to reach its first minimum after the merger. Then, we plot this against the mass-weighted tidal deformability, which is defined as

$$\tilde{\Lambda} = \frac{16}{3}\frac{(M_A + 12M_B)M_A^4\Lambda_A + (M_B + 12M_A)M_B^4\Lambda_B}{(M_A + M_B)^5}, \tag{3.1}$$

where Λ_A, Λ_B is the dimensionless tidal deformability for the two component of the binary.

Figure 3.2 shows $\Delta t_{\rm min}$ v.s $\tilde{\Lambda}$ We then fit the data using the relation:

$$\frac{\Delta t_{\rm min}}{M} = a\frac{1 + b\tilde{\Lambda}}{1 + c\tilde{\Lambda}}. \tag{3.2}$$

The least square fit yields these results:

$$a = 3.782 \times 10^1, b = 6.514 \times 10^{-4}, c = 6.064 \times 10^{-5}.$$

The GW signal after it reaches its first minimum, the amplitude starts to grow up until it reaches a new maximum. We find the relation between the value of this amplitude and the mass ratio of the binary, which is shown in Figure 3.3

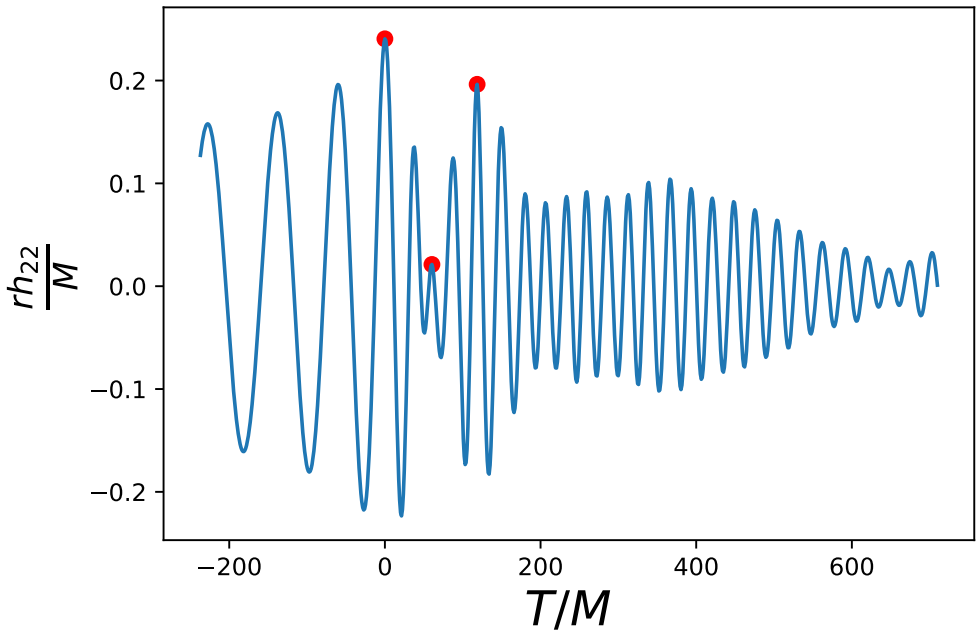

Figure 3.1: The GW signal for model THC:0003 of the CORE database. Red dots mark the merger, first post-merger minimum, and first post-merger maximum. Here, both time and amplitude are dimensionless.

Again we fit the data using the equation:

$$\frac{rh_{22}(t_{\max_1})}{M} = a\frac{1+bq}{1+cq}, \tag{3.3}$$

which yields:

$$a = 2.798 \times 10^{-1}, b = -5.384 \times 10^{-1}, c = -2.523 \times 10^{-1}.$$

3.2 Frequency Domain

We obtain the frequency domain by isolating the postmerger part of GW signal, then apply a Tukey window and finally taking the FFT (Fast Fourier Transformation). We can see an example at Figure 3.4 .

The main characteristic of this frequency spectrum is the peak which is known as f_2. In the paper [25] there is the definition for a parameter ζ which is a linear combination of k_{eff} ($k_{\text{eff}} = \frac{3}{16}\tilde{\Lambda}$) and $\frac{M}{M_{\text{TOV}}}$. M_{TOV} is the maximum allowed mass of a single non-rotating NS and is a therefore a characteristic of its EOS. The final formula for ζ is:

$$\zeta = k_{\text{eff}} + a\frac{M}{M_{\text{TOV}}}, \tag{3.4}$$

where $a = -131.7010$

The results of this analysis are show in Figure 3.5

Following the same way of thinking as in the Time Domain analysis we fit the results using:

$$Mf_2(\zeta) = a\frac{1+b\zeta}{1+c\zeta}. \tag{3.5}$$

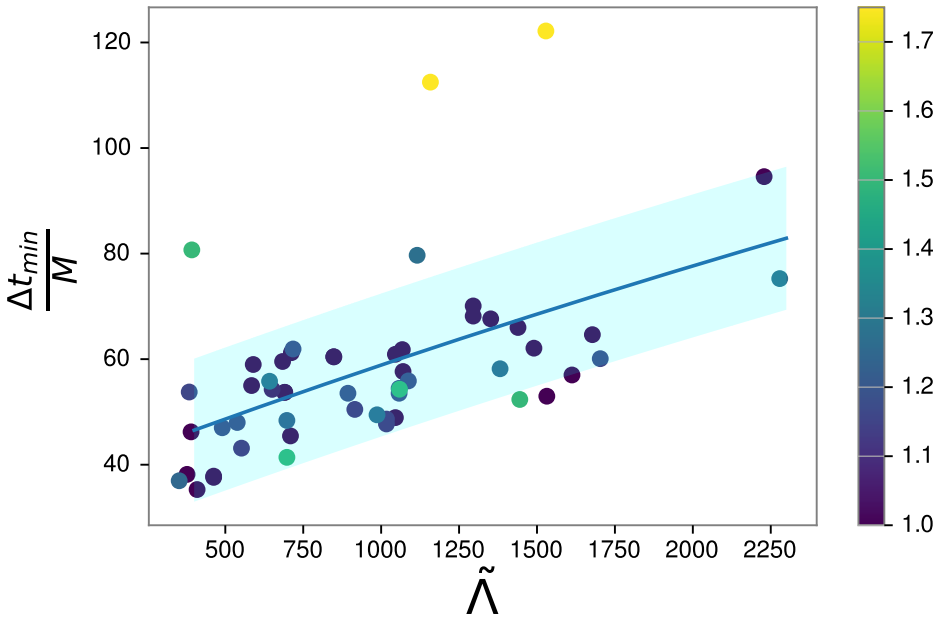

Figure 3.2: Dimensionless time between merger and the first postmerger minimum as a function of the dimensionless mass-weighted tidal deformability. The colors represent the different mass ratios

The least squares fit gives as a result:

$$a = 3.396 \times 10^{-2}, b = 1.927 \times 10^{-3}, c = 3.857 \times 10^{-3}.$$

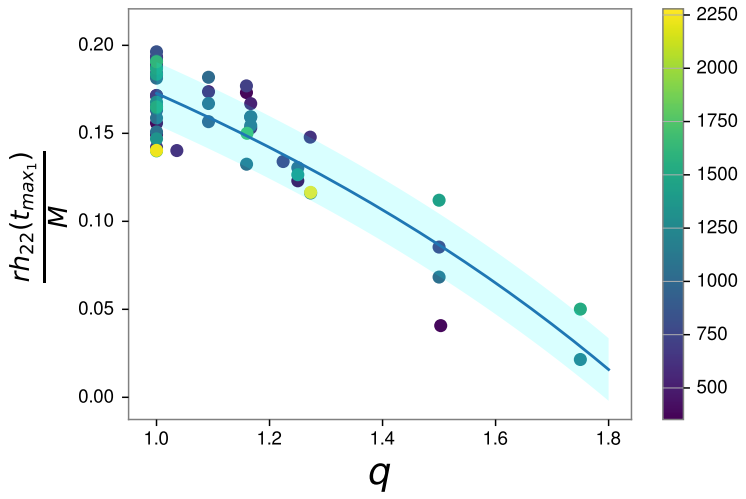

Figure 3.3: The first peak of the postmerger as a function of the mass ratio. The color represents the dimensionless mass weighted tidal deformability

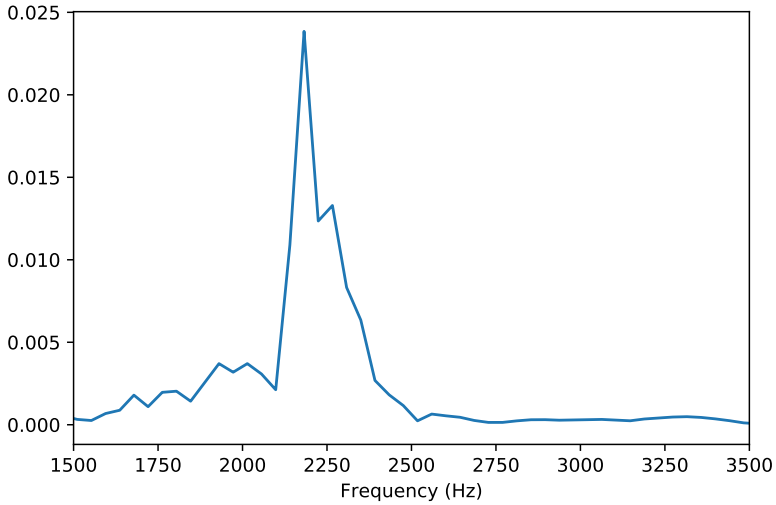

Figure 3.4: The frequency domain of the postmerger for THC:0001

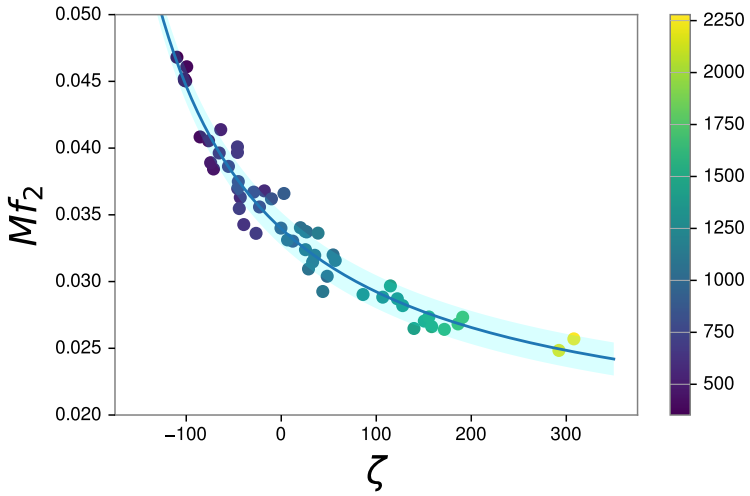

Figure 3.5: The dimensioness Mf_2 as function of ζ. The color shows the dimensionless mass weighted tidal deformability

Chapter 4

Spectral Classification of Post-Merger Gravitational Wave Emission

In this chapter we will explore the main frequencies presented in the postmerger spectrum of multiple simulations and we will try to do some sort of classification based on the shape of the spectrum they produce.

To date, the advanced GW detectors have only been able to observe the inspiral of NS mergers and no postmerger signals have been observed. This is caused due to the high emission frequency at which current GW detectors are less sensitive. Future detectors are expected to be more sensitive and allow us to detect the postmerger phase of a few loud events

4.1 Main frequencies

The frequency spectrum of the postmerger of GW signal has a characteristic peak which is known as the main postmerger frequency (f_{peak}). In addition to that there are two other low frequency secondary peaks ($f_{2-0}, f_{\text{spiral}}$). The first one is a nonlinear combination frequency between the dominant quadrupolar f_{peak} oscillation and the quasiradial oscillation of the remnant. More information about the nature of this secondary peak can be found in [26]. The second one is produced by the rotating pattern of a deformation of spiral shape. This deformation is initially produced at the time of merging and is then sustained for a few rotational periods. According to [27] these two mechanisms are independent and can be distinct. The secondary f_{spiral} peak is produced by a strong deformation initiated at the time of merging, the pattern of which then rotates slower than the inner remnant and lasts for a few rotational periods, while diminishing in amplitude.

The consideration of the two different mechanisms leads to a unified classification scheme for the postmerger dynamics and GW emission. For high-mass binaries (relative to the threshold mass to prompt black-hole collapse), the nonlinear combination frequency dominates, while for low-mass binaries it is the spiral deformation that produces the strongest secondary peak. Both are simultaneously present and can produce peaks of comparable strength for intermediate binary masses.

4.2 Type Classification

We use the same classification as in [27], which means that we have three types depending on the relative strength of f_{2-0} and $f_{\rm spiral}$. The three types can be described as it follows:

- Type I: When the total binary mass $M_{\rm tot}$ is not too far from the threshold mass for prompt quasiradial collapse of the remnant for a given EOS the evolution of the central lapse function is dominated by a very strong quasiradial oscillation of the remnant. For such models the two initial NSs are more centrally condensed, and they merge with higher impact velocity. Because of the strongly excited quasiradial oscillation, f_{2-0} is the strongest secondary peak in the GW spectrum, while $f_{\rm spiral}$ is much weaker, likely because for more compact NSs the formation of the spiral pattern is less pronounced.

- Type II: For intermediate total binary masses, f_{2-0} and $f_{\rm spiral}$ have a comparable strength in the GW spectrum and the two types of secondary peaks are well separated. In characteristic quantities such as the central lapse function, the low frequency modulation with f_{2-0} and $f_{\rm spiral}$ are clearly noticeable.

- Type III: When the total binary mass $M_{\rm tot}$ is significantly below the threshold mass for quasiradial collapse, the time evolution of the central lapse function is dominated by the $f_{\rm peak}$ and $f_{\rm spiral}$ modulation as a result of the rotating spiral pattern with the two antipodal bulges. In the evolution of the central lapse function, this modulation typically has a smaller amplitude than type-I variations. The smaller NS compactness also allows for a stronger spiral deformation. Consequently, the dominant secondary peak in the GW spectrum is $f_{\rm spiral}$, while f_{2-0} is either very weak or hidden inside the background.

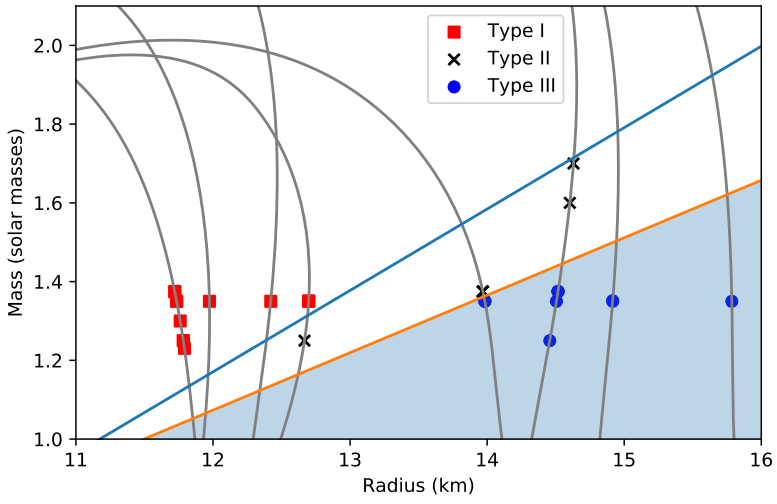

Figure 4.1: A representation of the different types on an $M(R)$ diagram. The lines that separate the figure into three sections come from [28]. The points come from the CoRe database and are for the cases that we explored in chapter 5.

This distinction may not always be clear, as there are many cases especially close to the borders of each type and for big mass ratios, that could potentially belong to

both or neither type. However for the majority of the mergers you can distinguish between the three types and see how for the same EOS you can go from type 3 to 1 as your stars get heavier.

4.3 Expected Frequencies

The question remains as to whether we can predict the frequencies at which the main and secondary peaks should be found. Following the work of [28] we have some equations we can use to make such predictions within range.
These empirical relations came from analyzing the CFC/SPH GW catalog for many different masses and EOS. Using a least-squares minimization method they constructed two-parameter relations of the form $f_j(R_x, M_{chirp})$ where j is one of the frequency peaks ($f_{\rm peak}$, f_{2-0}, $f_{\rm spiral}$) and x stands for the mass of fiducial nonrotating NS models, in solar masses. $M_{\rm chirp}$ is the chirp mass of the inspiraling binary. The set was divided to two, one being the binary systems with equal mass partners and the second one being the whole set including both equal and unequal mass binaries. This work was done in [28] and the equations are:

- For equal mass binary systems

$$\begin{aligned} f_{\rm peak}/M_{\rm chirp} =& 13.822 - 0.576 M_{\rm chirp} - 1.375 R_{1.6} + 0.479 M_{\rm chirp}^2 \\ & - 0.073 R_{1.6} M_{\rm chirp} + 0.044 R_{1.6}^2, \end{aligned} \tag{4.1}$$

$$\begin{aligned} f_{2-0}/M_{\rm chirp} =& 8.943 + 4.059 M_{\rm chirp} - 1.332 R_{1.6} - 0.358 M_{\rm chirp}^2 \\ & - 0.182 R_{1.6} M_{\rm chirp} + 0.048 R_{1.6}^2, \end{aligned} \tag{4.2}$$

$$\begin{aligned} f_{\rm spiral}/M_{\rm chirp} =& 6.264 + 1.929 M_{\rm chirp} - 0.645 R_{1.8} + 0.881 M_{\rm chirp}^2 \\ & - 0.311 R_{1.8} M_{\rm chirp} + 0.03 R_{1.8}^2. \end{aligned} \tag{4.3}$$

- For all binary systems (both equal mass and not)

$$\begin{aligned} f_{\rm peak}/M_{\rm chirp} =& 10.942 - 0.369 M_{\rm chirp} - 0.987 R_{1.8} + 1.095 M_{\rm chirp}^2 \\ & - 0.201 R_{1.8} M_{\rm chirp} + 0.036 R_{1.8}^2, \end{aligned} \tag{4.4}$$

$$\begin{aligned} f_{2-0}/M_{\rm chirp} =& 9.586 + 4.09 M_{\rm chirp} - 1.427 R_{1.6} + 0.048 M_{\rm chirp}^2 \\ & - 0.261 R_{1.6} M_{\rm chirp} + 0.055 R_{1.6}^2, \end{aligned} \tag{4.5}$$

$$\begin{aligned} f_{\rm spiral}/M_{\rm chirp} =& 5.846 + 1.75 M_{\rm chirp} - 0.555 R_{1.8} + 1.002 M_{\rm chirp}^2 \\ & - 0.316 R_{1.8} M_{\rm chirp} + 0.026 R_{1.8}^2. \end{aligned} \tag{4.6}$$

In all equations mass is given in solar masses and the radius for the various masses is given in kilometers (km). The frequency is calculated in kHz.

This set of equations can be used to predict the frequency at which the main and secondary peaks of the postmerger GW spectrum should appear. In [28] the simulations used to extract these relations came from CFC/SPH GW catalog. In the next chapter we will investigate if these relations can be used in three other catalogs.

Chapter 5

Frequency Plots

In this chapter we will discuss the analysis of the postmerger frequency spectrum from three catalogs. The analysis was done using python codes to isolate the postmerger part of the time domain, then FFT in order to get the frequency domain. After that we used the equations described in chapter 4 in order to get the frequencies in which we expect to get the main and secondary peaks. After that we did some plotting in order to visualize our results and get a picture of how close are the expected frequencies to the actual peaks. Finally we produced the spectrograms using wavelets in order to visualize the time evolution of the frequency peaks.

This work was done for multiple simulations from each catalog and the results are available in (https://github.com/johnkou97). For this thesis we picked a few cases in order to be able to discuss the results.

We also added an extra line for an expected secondary peak in higher frequencies than the main peak. The new (2+0)peak is symmetrical to the f_{2-0} with respect to the main peak and is given by the equation:

$$f_{2+0} = 2f_{\text{peak}} - f_{2-0}. \tag{5.1}$$

We will use this line to test if it coincides with a local maxima of the frequency spectrum.

5.1 CoRe

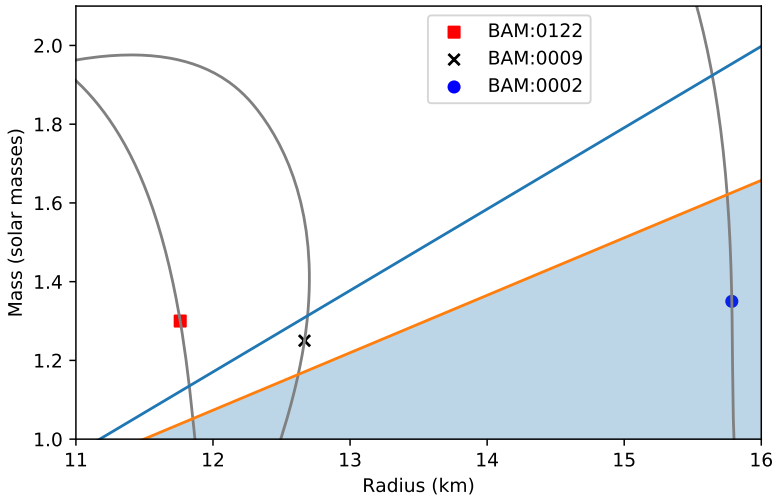

Figure 5.1: The three mergers from the CoRe catalog that will be discussed in this chapter. We can clearly see that they represent all three types as discussed in chapter 4. For more information about this type of figure you can see 4.1.

The CoRe data [25] are available at (`www.computational-relativity.org`). We selected 31 simulations from the BAM catalog in order to create the plots. The full results are available here: (`http://github.com/johnkou97/postmerger_frequencies/tree/master/results`). We will discuss three cases, one from each type and also see if the peaks appear in the frequencies we expect them. Some numerical results are available in Table B.1.

The first case we study is the simulation BAM:0122 . The characteristics of the system can be found in Appendix B. It was selected because it is a great example of a Type I merger. We can clearly see the dominant peak in all Figures 5.2 to 5.4. Moreover there is a clear secondary peak at around 2 kHz. From our analysis of the three types and knowing that BAM:0122 is of the first type, due to the masses and the EOS of the two neutron stars, we should expect that it comes from the non linear combination frequency f_{2-0}. If we calculate the frequencies at which we expect the secondary peaks to appear, from Equations (4.5) and (4.6), we get the lines that are shown in Figures 5.2 and 5.3. The line for the 2-0 secondary peak is much closer to the actual peak leading us to assume that it is indeed the f_{2-0} that is more dominant. The (2+0) line also falls in accordance with a local maximum, a very strong indication that the actual peak there is indeed the f_{2+0}.

After our discussion about the type of the merger and the secondary peaks, we produced the spectrogram fig. 5.4 in order to see the time evolution of the frequency spectrum. We used wavelets in order to produce this figure. Wavelets have two main characteristics. First one is the width which is the frequency resolution, and bandwidths which describes the time resolution. Of cource if the time resolution is too high there is the risk of not getting a really accurate picture on the frequency domain because we analyze a smaller part of the signal. This technique will be used to produce all the spectrograms that appear on this thesis.

For BAM:0122 we can see that the main peak has a strong presence in most of

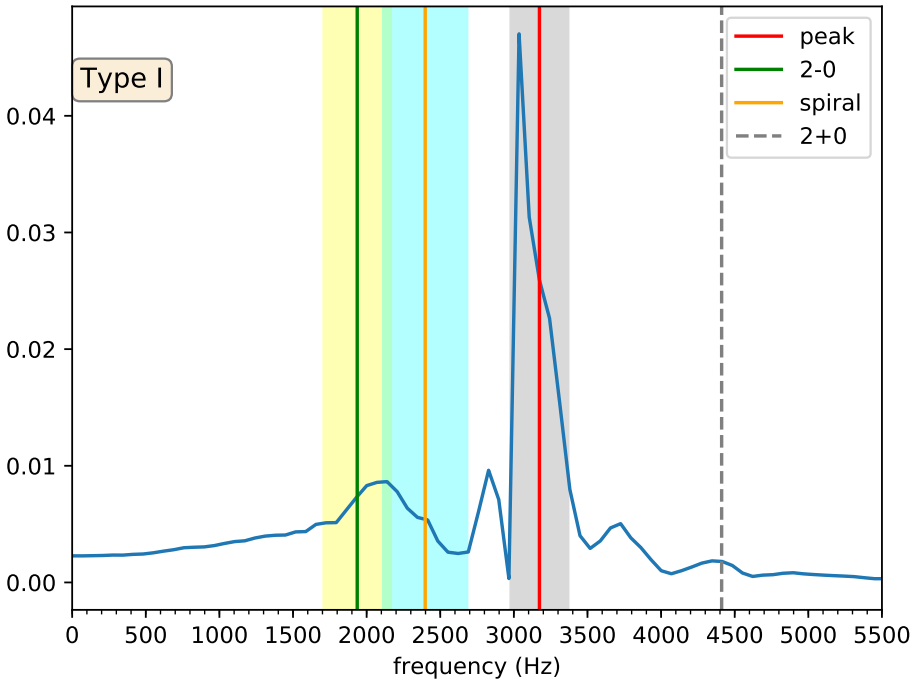

Figure 5.2: The linear frequency plot for BAM:0122. It is a type I binary neutron star merger as we can see from the dominant secondary peak which is the non linear combination frequency f_{2-0}.

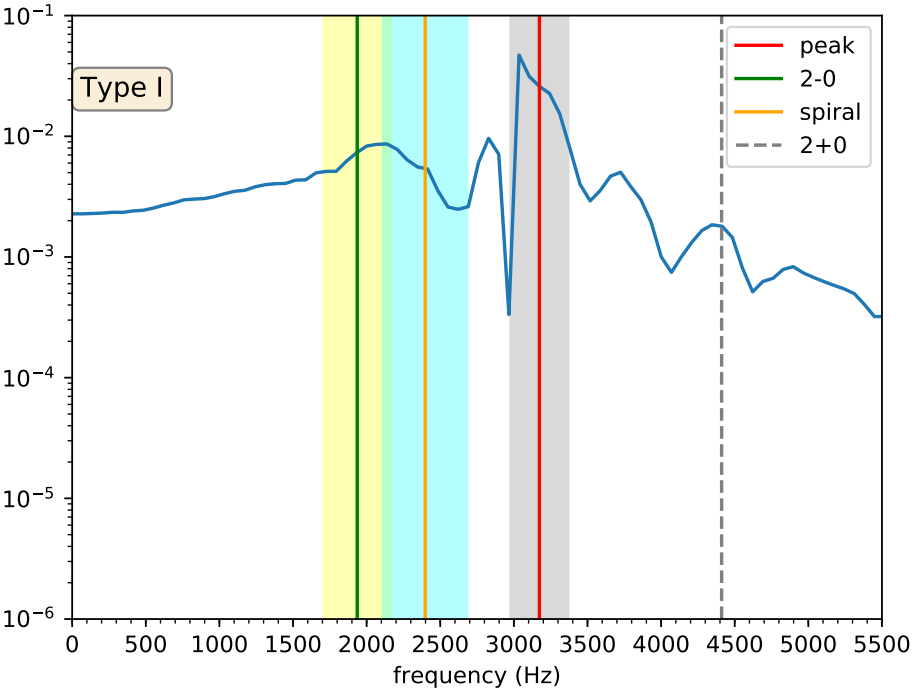

Figure 5.3: Again the BAM:0122 in logarithmic scale.

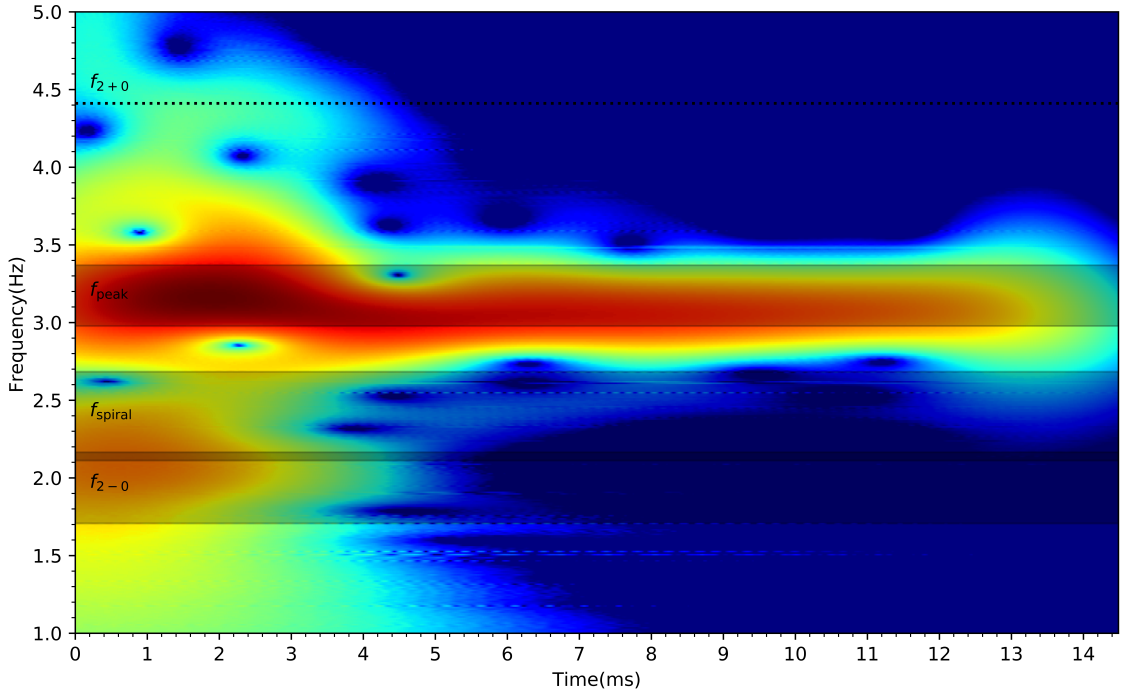

Figure 5.4: The spectrogram of BAM:0122. We can clearly see the main peak and also a secondary peak at arounf 2 kHz.

the timeseries. It has a bigger amplitude in the first few miliseconds, then slowly diminishes until the end of the postmerger phase. On the other hand the secondary peak is only present for a few miliseconds. This was expected due to the nature of the mechanisms producing this peak as discussed in chapter 4. After this initial bump, the amplitude of the secondary peak vanishes and is no longer present in the later stages of the postmerger.

The next case we will discuss is BAM:0009. Again you can find more about the system at Table B.1. We selected this case because it is a typical Type II binary neutron star merger. The figures are shown here: Figures 5.5 and 5.6. As in all postmerger frequency spectrums we have the main peak. At smaller frequencys we can clearly see the two secondary peaks. As we have previously discussed in chapter 4 the Type II spectrum should consist of two distinguished secondary peaks with more or less the same amplitude. The f_{2+0} line falls between two high frequency peaks, which makes it not possible to say which peak is actually the (2+0) frequency.

The logarithmic scale helps us a bit more to seperate the two secondary peaks. We can see that we have a satisfying agreement between our lines and the actual peaks of the spectrum, with only the exception of f_{peak} which is in a bit lower frequency than expected .Especially in the secondary peaks, our lines are showing the position of each peak, helping us distinguish between f_{2-0} and f_{spiral}.

In the spectrogram fig. 5.7 we can have a clear view of the secondary peaks. We can see the two bulges, one of which is a bit above 1.5kHz and the second one a bit lower. We also see how both are only affecting the timeseries for the first few miliseconds, in contrary with the main peak which is affecting almost the whole

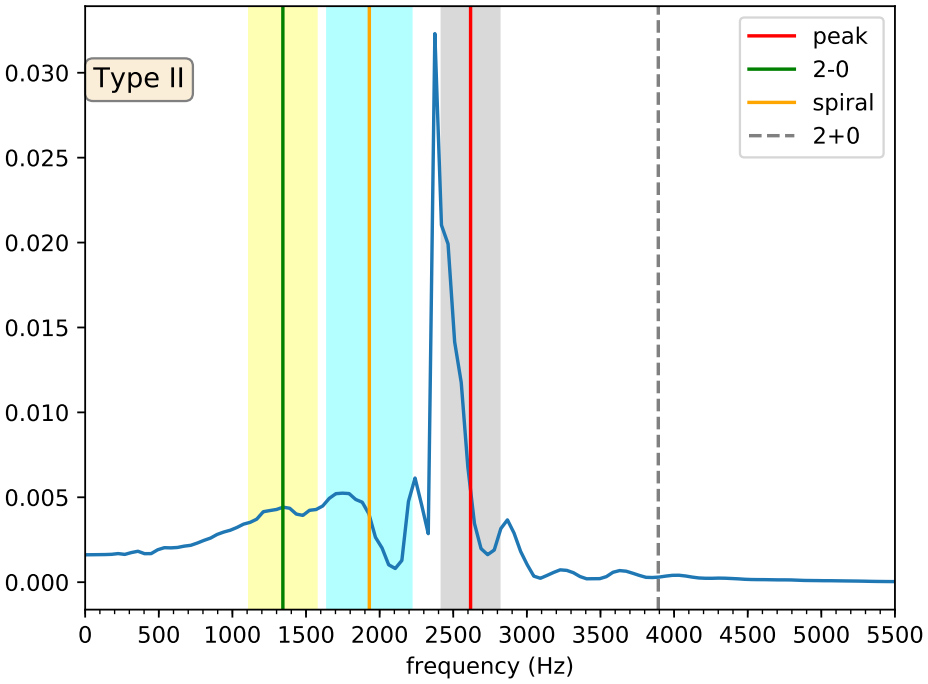

Figure 5.5: The linear frequency plot for BAM:0009. It is a type II binary neutron star merger as we can see from the fact that the inspiral and 2-0 frequency amplitudes are at the same level.

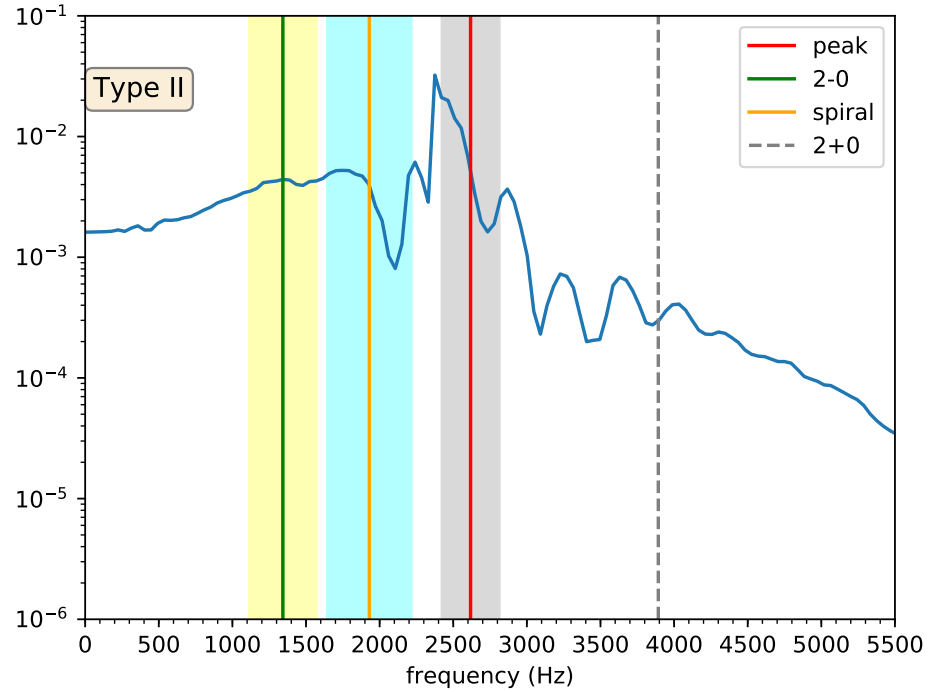

Figure 5.6: The frequency spectrum for BAM:0009 in logarithmic scale.

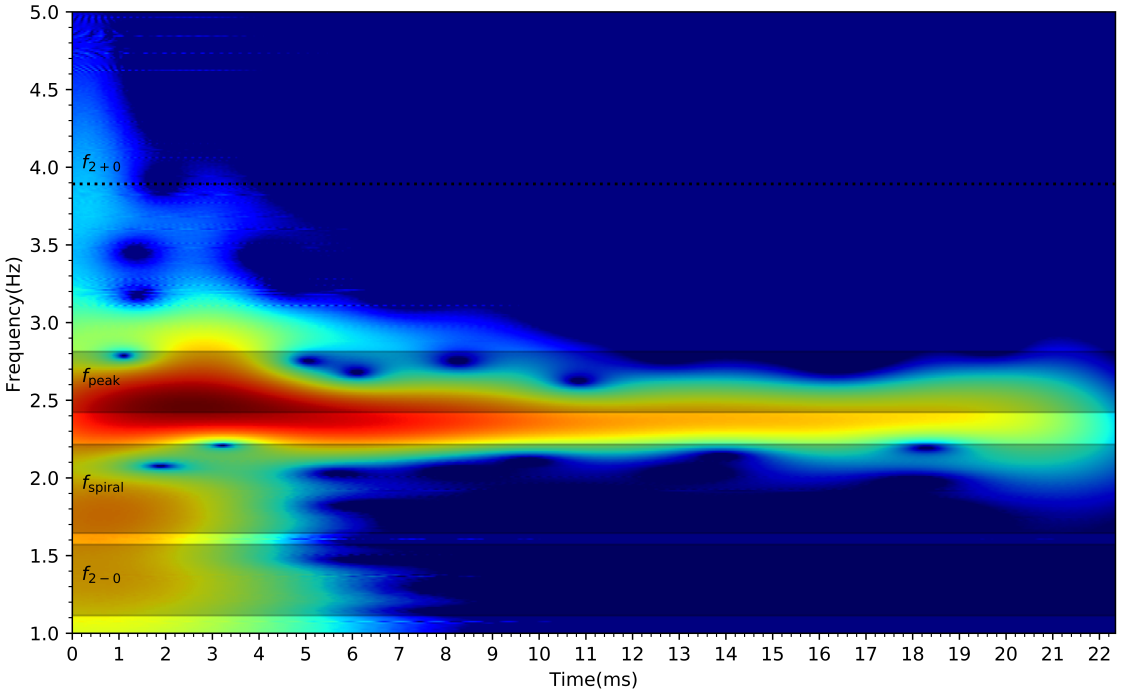

Figure 5.7: The spectrogram of BAM:0009. We can clearly see the main peak and also the two distinguished secondary peaks.

timeseries.

After that we focus on BAM:0002. Again we can see the characteristics of the binary system at Table B.1. For this system we have $q = 1$ meaning that the masses of the two neutron stars are equal and thus we can use the Equations (4.4) to (4.6). From [28] we expect that this set of equations provides a more accurate description of the main and secondary peaks, having a smaller RMS error, and we choose to use them when possible.

From the masses and EOS of the two neutron stars we expect a type III merger, meaning that the postmerger spectrum should have the f_{spiral} as the most dominant from the two secondary peaks. We can see the Figures 5.8 and 5.9. As expected the FFT of the Time Domain gives us the main peak and a clear secondary peak. The other secondary peak is not obvious, because of its small amplitude. Drawing the lines from the equations mentioned, the f_{spiral} falls into agreement with the secondary peak with great accuracy. We also have an agreement with the main peak, but with some error. All of these information agree with our classification of the merger as type III. This is actually a great example because f_{spiral} is so dominant in compare to f_{2-0}. Moreover the agreement of our expected frequency with the actual peak is great, telling us that it is indeed the inspiral and also confirming the equations from [28]. The f_{2+0} fails to find a high frequency peak, which is something to be expected since the (2-0) secondary peak is not relevant for this case.

Lastly we want to see the spectrogram. In fig. 5.10 we can see the main peak and one secondary peak. As in all the previous mergers, the main peak has an effect on all the postmerger time domain. The secondary peak (in this case the inspiral)

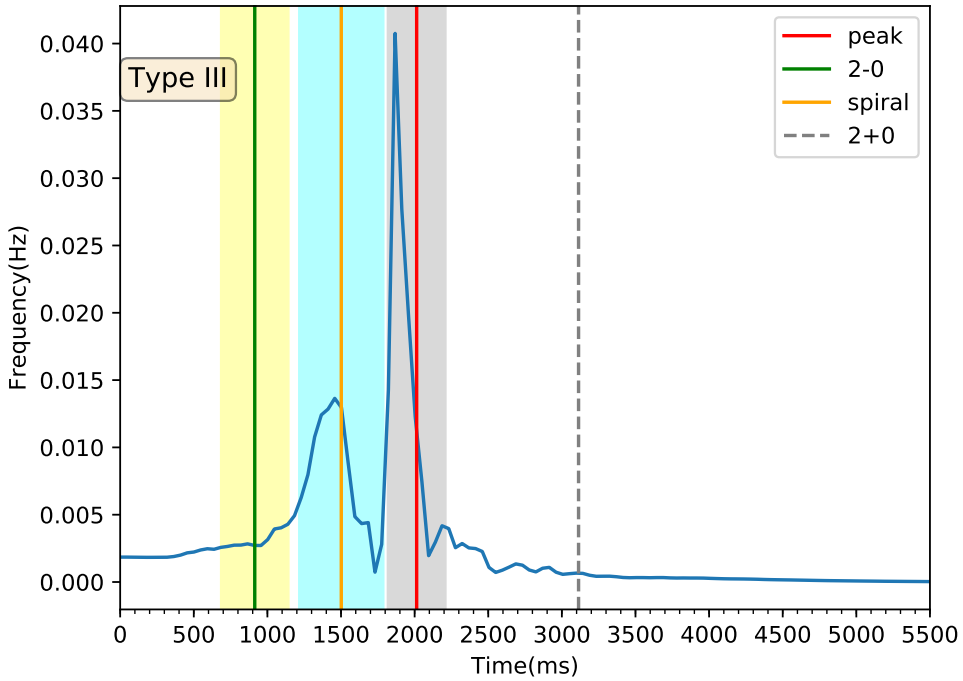

Figure 5.8: The linear frequency plot for BAM:0002. It is a type III binary neutron star merger as we can see from the dominant secondary peak which is the inspiral f_{spiral}. The lines come from Equations (4.4) to (4.6), for $q = 1$ because the masses of the binary system are equal.

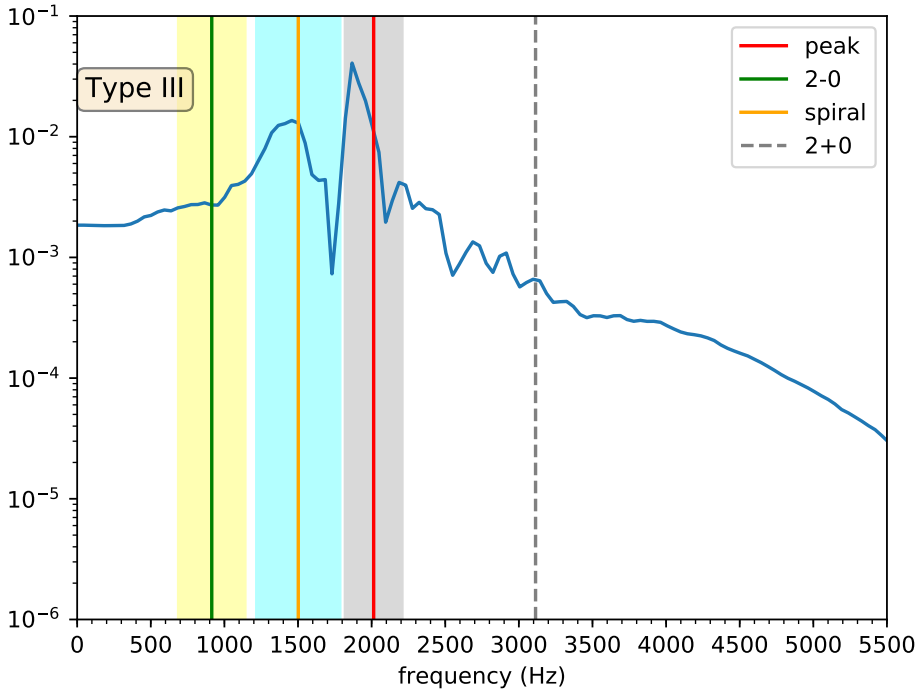

Figure 5.9: A logarithmic view of the BAM:0002 frequency spectrum.

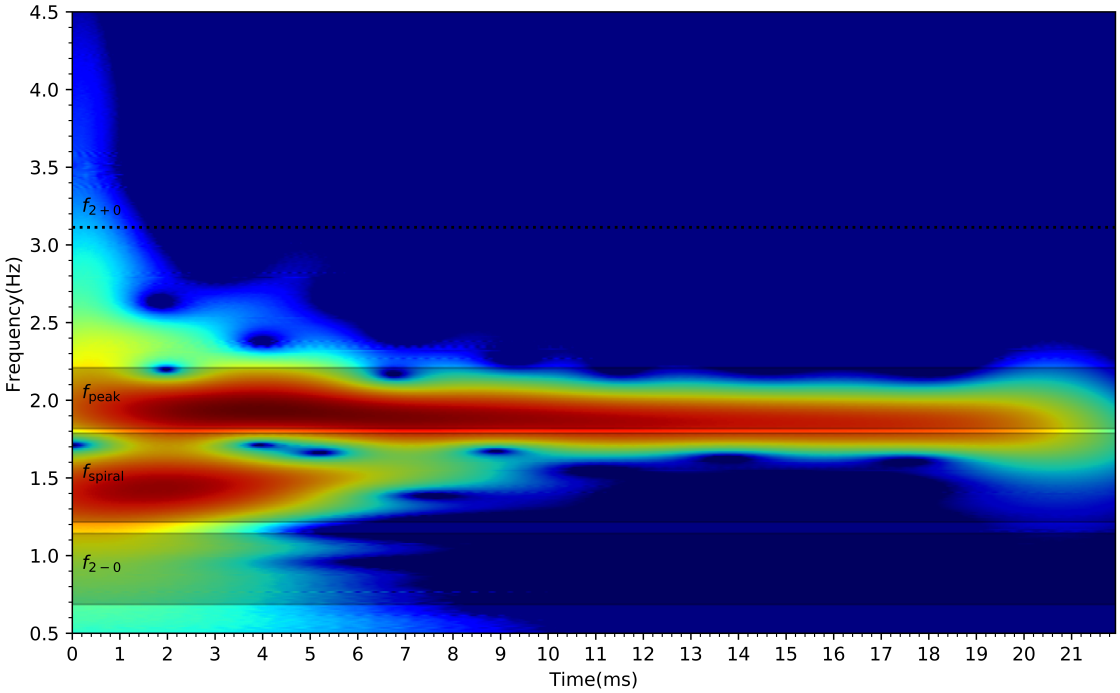

Figure 5.10: The spectrogram of BAM:0002. There are two obvious peaks, one is the dominant main peak and the second is the inspiral secondary peak

only affects the first few milliseconds, and thus appears with smaller amplitude on the frequency spectrum fig. 5.8.

5.2 Sacra

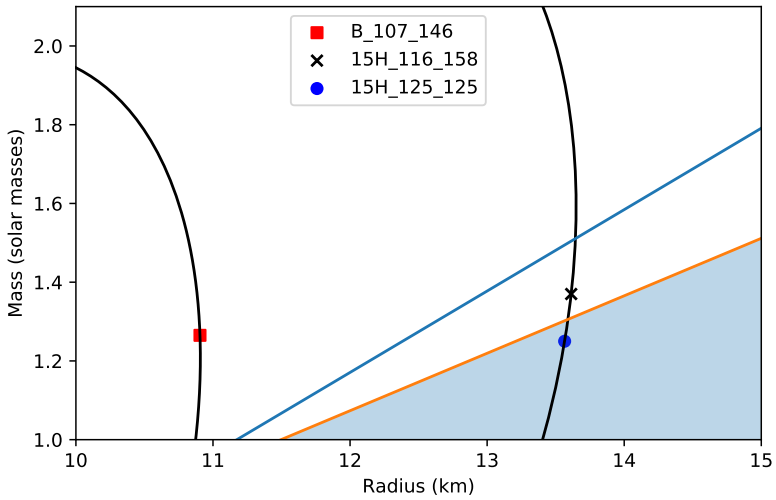

Figure 5.11: The three mergers from the Sacra catalog that will be discussed in this chapter. We can clearly see that they represent all three types as discussed in chapter 4. For more information about this type of figure you can see 4.1.

The SACRA Gravitational Waveform Data Bank [29] is available at (`http://www2.yukawa.kyoto-u.ac.jp/~nr_kyoto/SACRA_PUB/catalog.html`). We analyzed the whole catalog and produced the results in the same fashion as we did with CoRe catalog. We have the $M(R)$ diagram of the whole set at fig. C.1.Again we will present three cases one from each type. Informations about the whole catalog can be found in Table C.2.

The names of the different simulations on this catalog are in the form of EOS_mass1_mass2, so for example when we see 125H_112_140 it means that the EOS is 125H and that the system has $M_1 = 1.12M_\odot$ and $M_2 = 1.40M_\odot$

The EOS used in this catalog are a bit different from the ones described in chapter 2. They also use piecewise polytropic EOS but with less parameters. The polytropic equation is:

$$P = \begin{cases} K_0\rho^{\Gamma_0} & \text{if } \rho_0 \leq \rho < \rho_1 \\ K_1\rho^{\Gamma_1} & \text{if } \rho_1 \leq \rho, \end{cases} \tag{5.2}$$

where ρ is the rest-mass density, P is the pressure, K_0 and K_1 are a polytropic constant, and Γ_0 and Γ_1 are an adiabatic index. At the boundary of these two piecewise polytropes, $\rho = \rho_1$, the pressure is required to be continuous $K_0\rho_1^{\Gamma_0} = K_1\rho_1^{\Gamma_0}$, thus the parameters, which have to be given are $K_0, \rho_1, \Gamma_0, \Gamma_1$.

This process is described in detail at [29]. It was chosen to have a fixed low-density part with $\Gamma_0 = 1.3562395$ and $K_0 = 3.594 \times 10^{13}$ in cgs units. Also the adiabatic index for the high density part was chosen to be $\Gamma_1 = 3$ leaving K_1 to be defined from: $K_1 = K_0\rho_1^{\Gamma_0-\Gamma_1}$. Lastly the value of ρ_1 is what defines each different EOS in this catalog.

You can see the values of the densities at Table C.1. For more informations about the EOS used in this catalog you can read [30].

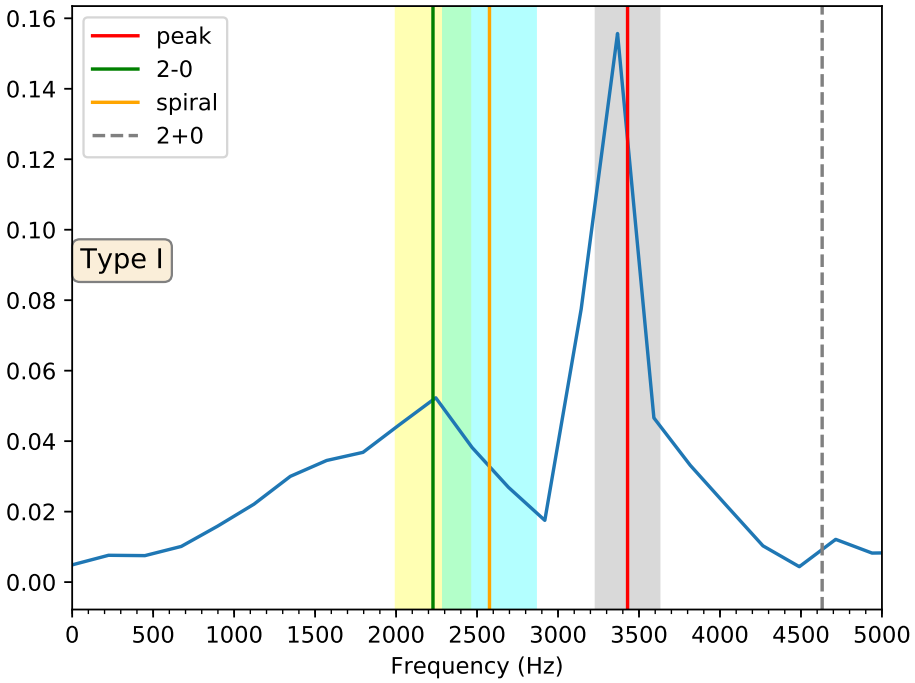

Figure 5.12: The linear frequency plot for B_107_146. It is a type I binary neutron star merger as we can see from the dominant secondary peak which is the non linear combination frequency f_{2-0}.

The first simulation is B_107_146 . We can see the postmerger frequency spectrum in fig. 5.12. Being a typical Type I merger, we have the f_{2-0} as the most dominant of the secondary peaks. The inspiral peak is not visible, because it gets covered by the nonlinear combination frequency. This is also obvious on the logarithmic scale (fig. 5.13).

The prediction of the f_{peak} and f_{2-0} is really accurate. Especially for the f_{2-0}, the fact that it falls exactly on the actual peak, helps us be sure that it is indeed the (2-0) and not the inspiral. For the f_{2+0} in this case, we can see a clear peak at around 4.7 kHz, which is predicted by our line.

The spectrogram (fig. 5.14) confirms all the observations from the frequency figures. We can clearly see one secondary peak at around 2.2 kHz. The main peak is spreading through the whole postmerger phase, while the secondary peak is only relevant in the early stages.

The next simulation from this catalog we will analyze is 15H_116_158 . As before we have the characteristics of the system at Table C.2. In this Type II postmerger spectrum we have two equally important secondary peaks (fig. 5.15). They are both covered from our predictions with good accuracy making it easy to distinguish between the two. The logarithmic scale in fig. 5.16 makes it a bit easier to separate the two independent secondary peaks. We can also see that the expected f_{peak} falls a bit off the actual peak but we still get the area at which we expect to find it. The dashed line for the (2+0) frequency is very close to an actual peak in the postmerger spectrum. It becomes even more apparent in the logarithmic scale.

The spectrogram at fig. 5.17 although not clear shows that there are indeed two

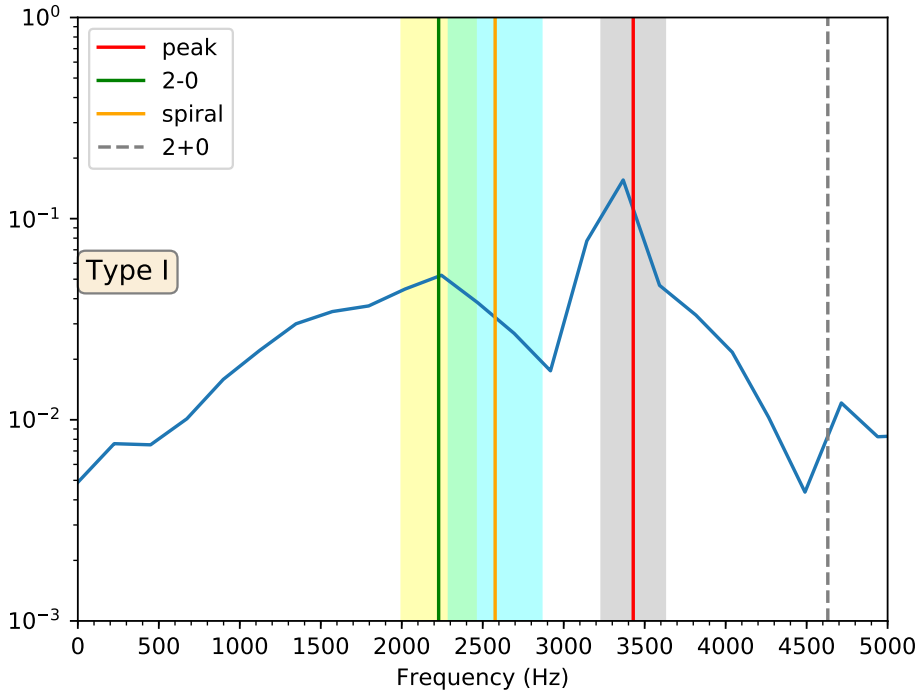

Figure 5.13: Again the B_107_146 in logarithmic scale

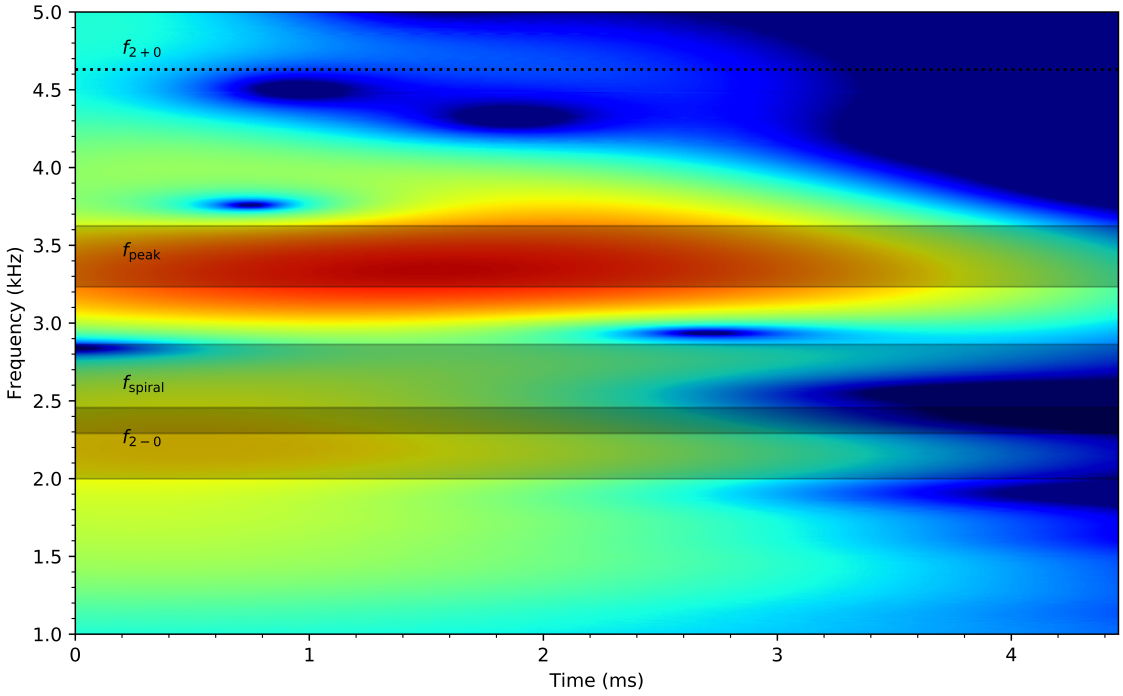

Figure 5.14: The spectrogram of B_107_146. We can clearly see the main peak and also one secondary peak above 2 kHz .

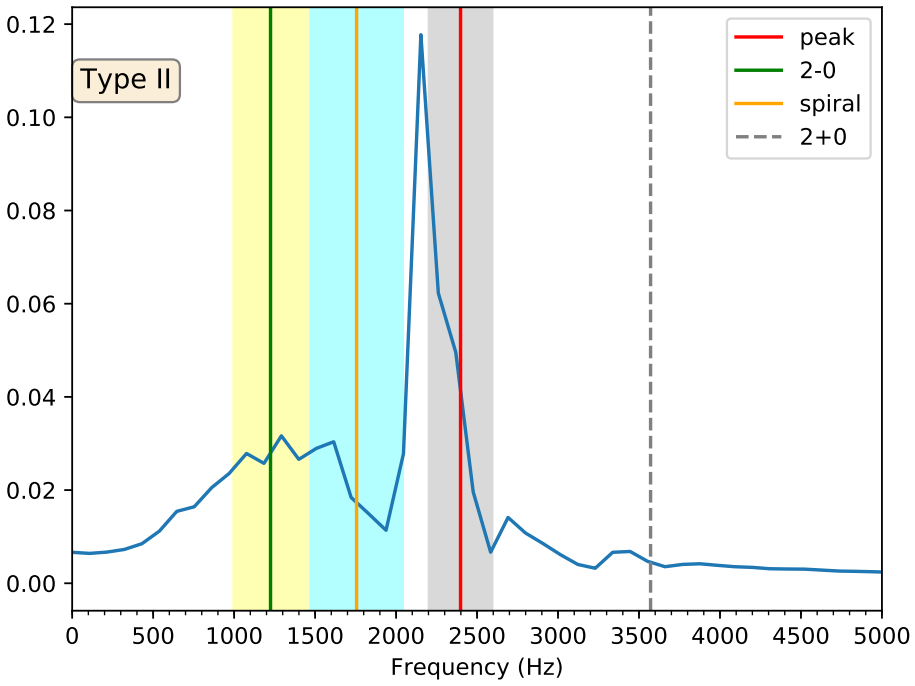

Figure 5.15: The linear frequency plot for 15H_116_158. It is a type II binary neutron star merger. The level of the inspiral and 2-0 secondary peaks are almost equal.

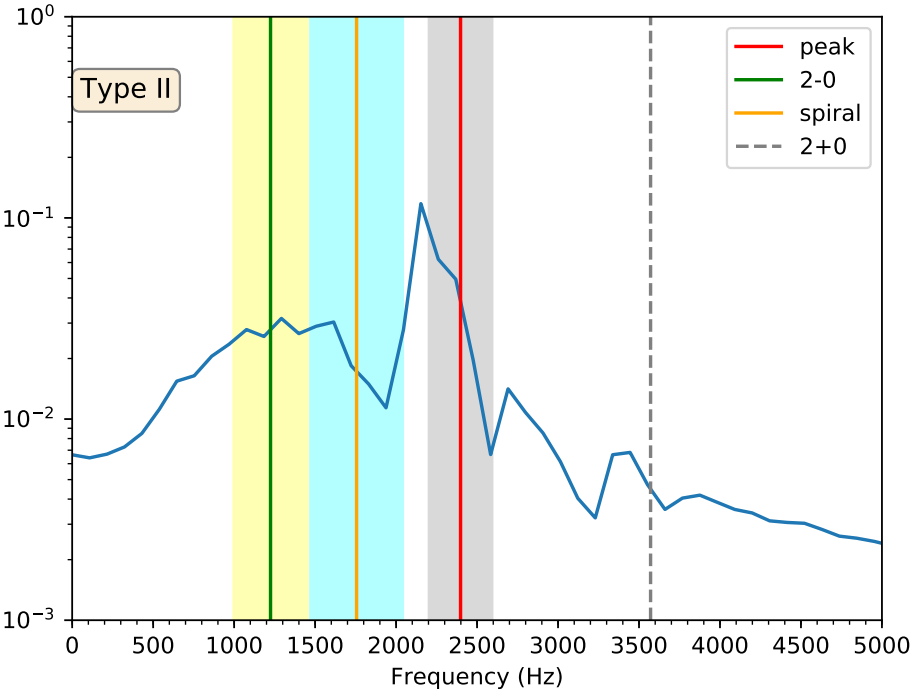

Figure 5.16: The frequency spectrum for 15H_116_158 in logarithmic scale.

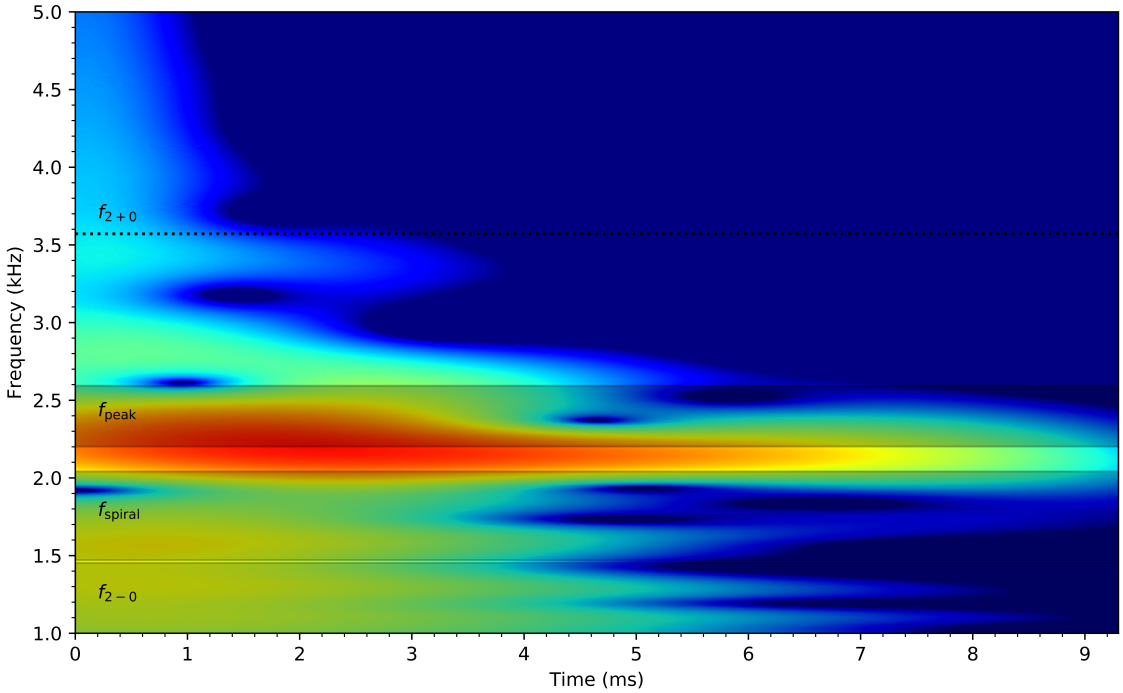

Figure 5.17: The spectrogram of 15H_116_158.

individual secondary peaks. This confirms that it is actually a Type II merger as we expect from our classification and the $M(R)$ diagram at fig. 5.11. We can also see a small peak at around 3.5 kHz, where the (2+0) secondary peak should appear.

The last waveform from the Sacra catalog that will be discussed in this thesis is 15H_125_125 . We can see the fourier plots in Figures 5.18 and 5.19. We see the main peak and one obious secondary peak. We can identify this peak as the inspiral because it is exactly where we would expect the f_{spiral} to be. The f_{2-0} line finds a small peak which becomes more clear in the logarithmic scale. As a Type III postmerger spectrum we expect the inspiral to be more dominant than the nonlinear combination frequency. This binary has a mass ratio of 1 meaning we can use the equations for $q = 1$ (Equations (4.4) to (4.6)). The accuracy for this case is great, especially on the secondary peaks, being able to accurately predict the frequency for even the dim (2-0) peak. The f_{2+0} line falls near a local maximum, although due to the lack of accuracy we can not be certain that this peak is actually the (2+0) peak predicted by the eq. (5.1)

The spectrogram at fig. 5.20 shows the same picture. We can see how the inspiral frequency is only relevant for almost 4 milliseconds, while the main peak is still strong at 11 to 12 milliseconds.

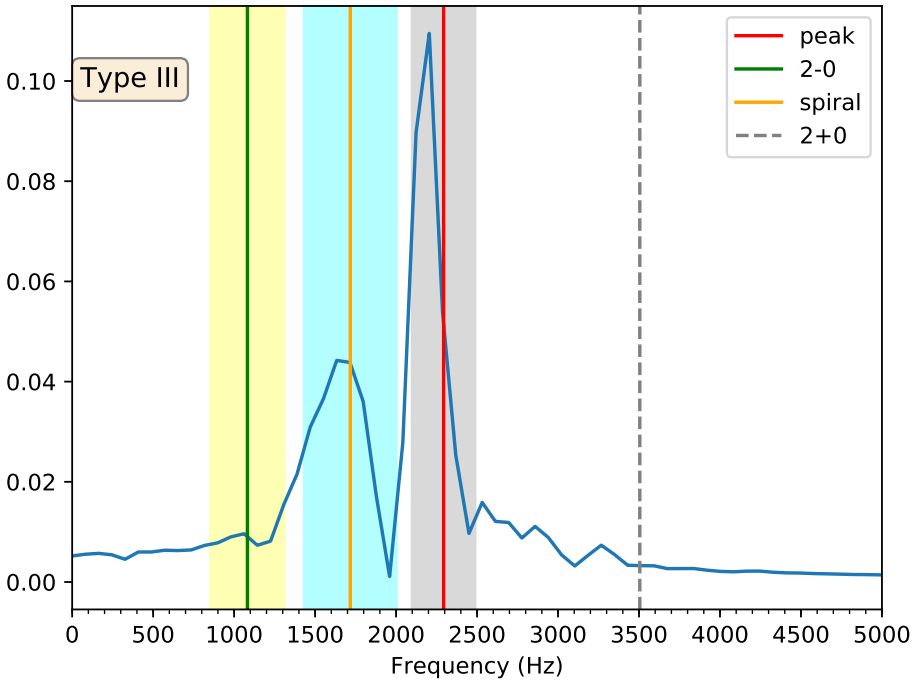

Figure 5.18: The linear frequency plot for 15H_125_125. It is a type III binary neutron star merger as we can see from the dominant secondary peak which is the inspiral f_{spiral}. The lines come from Equations (4.4) to (4.6), for $q = 1$ because the masses of the binary system are equal.

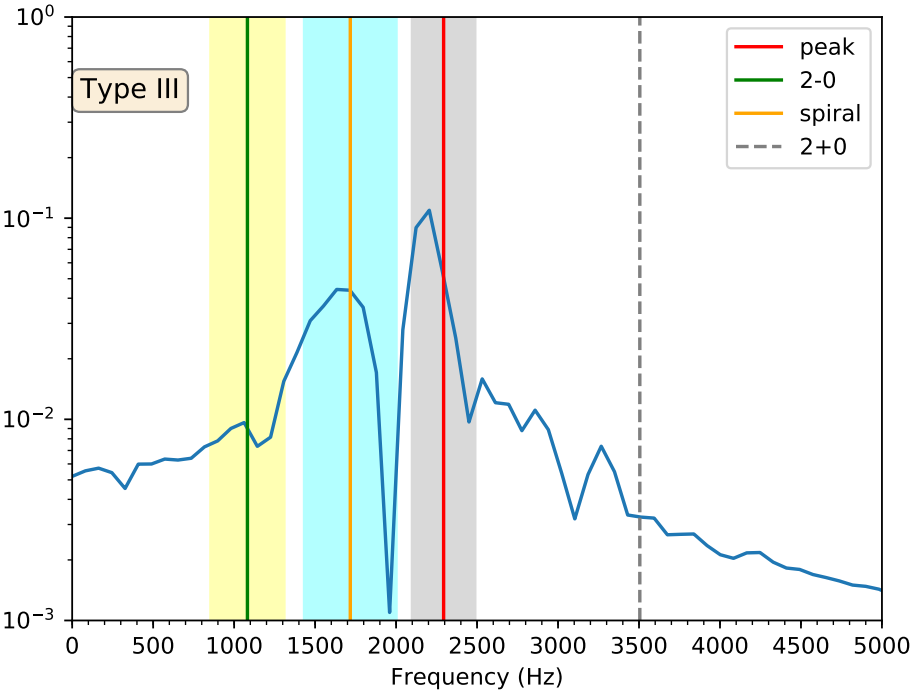

Figure 5.19: A logarithmic view of the 15H_125_125 frequency spectrum.

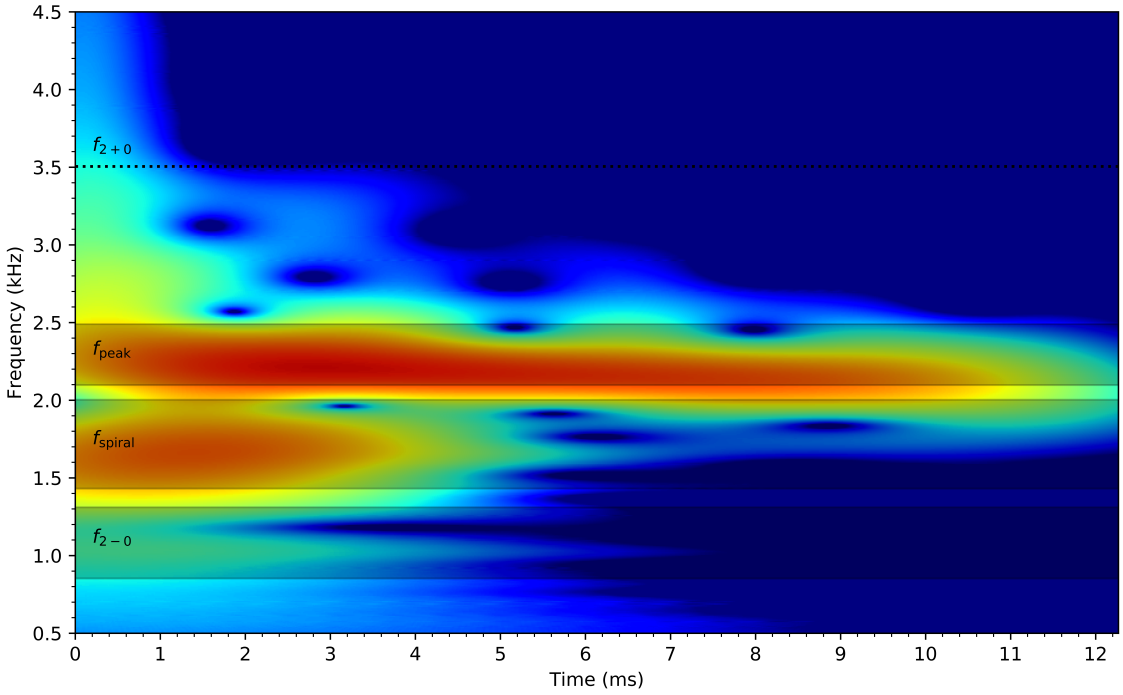

Figure 5.20: The spectrogram of 15H_125_125. There is only one visible secondary peak, which as discussed is the f_{spir}

5.3 Takami and Rezzolla

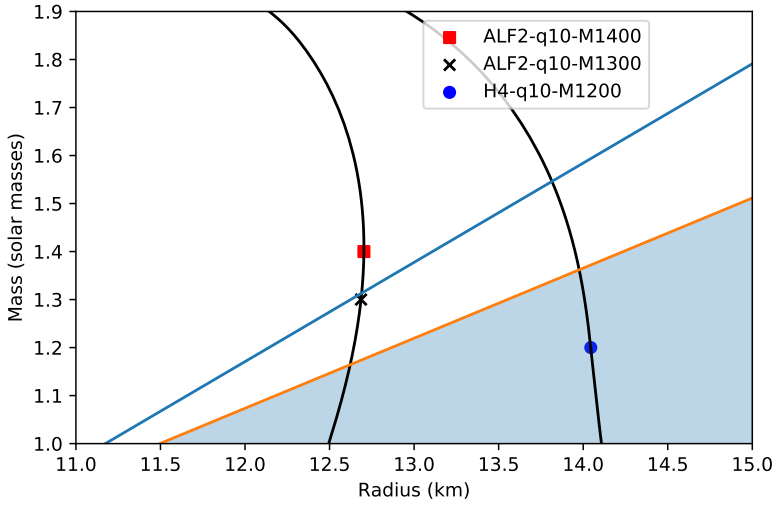

Figure 5.21: The three mergers from the Takami and Rezzolla catalog that will be discussed in this chapter. We can clearly see that they represent all three types as discussed in chapter 4. For more information about this type of figure you can see 4.1

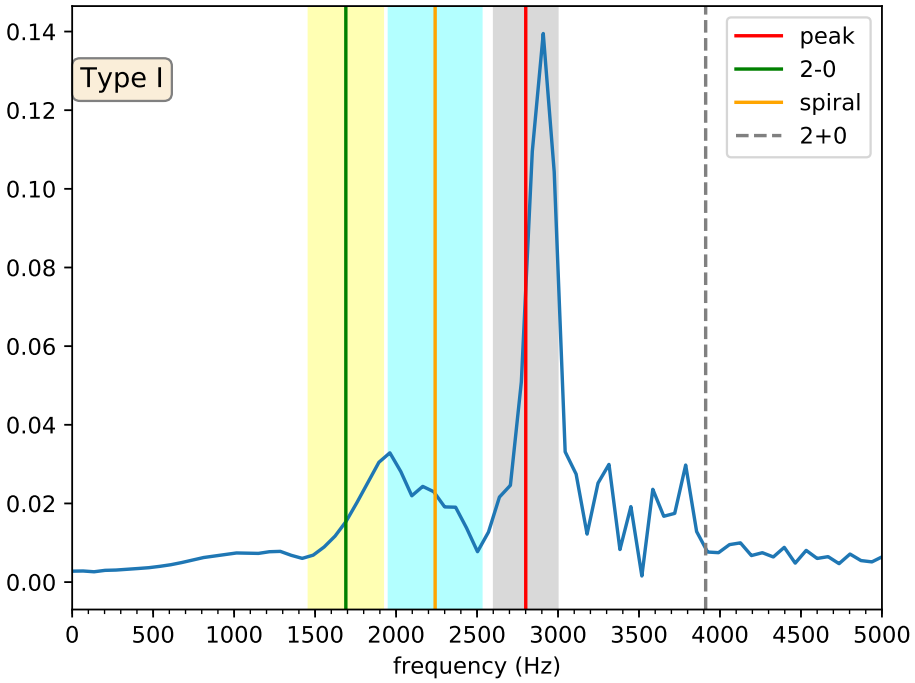

Figure 5.22: The linear frequency plot for ALF2-q10-M1400. It is a type I binary neutron star merger. The f_{2-0} has bigger amplitude than the f_{spiral}

The Gravitational-Waveform Catalog [31] from Luciano Rezzolla and Kentaro Takami is available at (`http://www.kobe-kosen.ac.jp/~takami/KTakami/contents/research/public_data/GW_Catalog/GW_Catalog_en.html`). We analyzed the whole catalog and produced the results in the same fashion as we did with the previous catalogs. The $M(R)$ diagram of the whole catalog is at fig. D.1.We will present, as before, three cases, one from each type. Informations about the whole catalog can be found in table D.1

The names of the different simulations of the catalog are in the form of EOS-q-Mass meaning that the simulation named SLy-q10-M1200 has the EOS of SLy, with mass ratio $q = 1$ and the mass of the first member of the binary system is $M_1 = 1.2M_\odot$

The first simulation from this catalog that will be presented is ALF2-q10-M1400 . From the masses and EOS of the system we should expect a type I merger meaning that the f_{2-0} will be the most dominant of the low frequency secondary peaks. It is also a $q = 1$ case which means we can use Equations (4.4) to (4.6) for our lines. We can see the results of the analysis on Figures 5.22 and 5.23. We find one really dominant secondary peak (after the main peak) which should be the (2-0). As we see the lines can't tell us which of the two is, however the line for the f_{spir} accurately predicts one smaller but visible peak and this leads us to assume that the dominant secondary peak is indeed the nonlinear combination frequency.

On the spectrogram at fig. 5.24 we have more evidence to support our claim that the f_{2-0} is the secondary peak with the biggest amplitude. We find two secondary peaks, from which the first appears to have bigger amplitude and the second is clearly noticeable but smaller. This is the typical picture of a type I postmerger

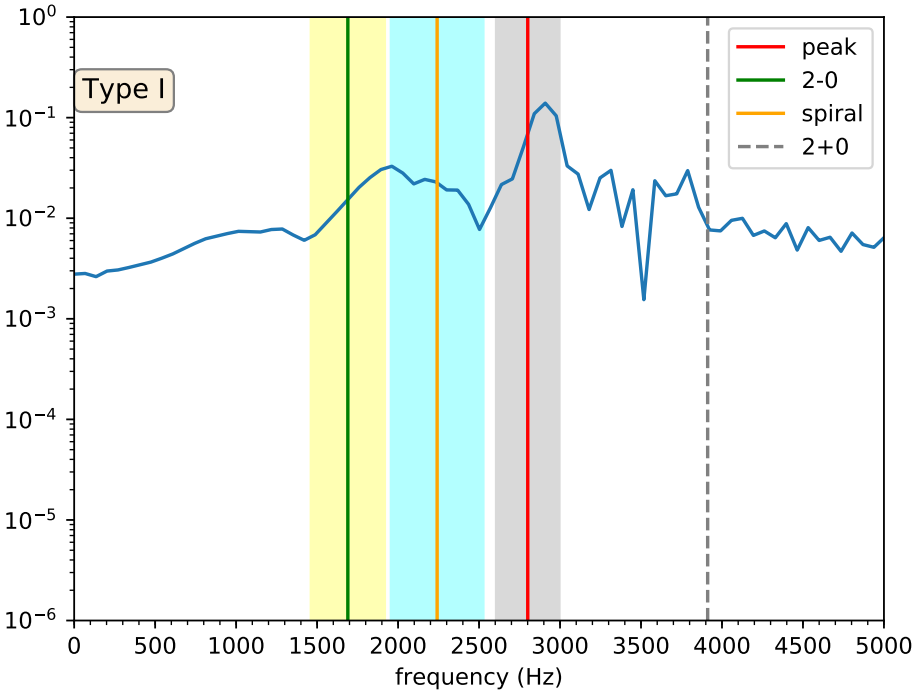

Figure 5.23: Again the ALF2-q10-M1400 in logarithmic scale

spectrogram, because (2-0) frequency peaks are in lower frequencies than the inspiral. In this spectrogram we see that the main peak behaves in bit of a peculiar way. At around 6 milliseconds after the merger, it starts to spread at higher frequencies.

On the second simulation we have ALF2-q10-M1300. We have once more a mass ratio of 1 so we employ Equations (4.4) to (4.6). The results of the analysis are shown in Figures 5.25 and 5.26.

We should expect a type II merger as we can see at our diagram in fig. 5.21. Indeed we find the two secondary peaks and although $f_{\rm spiral}$ has a bigger amplitude, we can see that they are both comparable. Especially on the logaritmic plot it is obvious that there is not a huge gap between the two. One more thing that should be noted is the great accuracy we get between the expected frequencies and the actual peaks for this simulation. Also the line for the (2+0) high frequency secondary peak falls exactly on a local maximum of the postmerger frequency spectrum. It is best shown on the log scale at fig. 5.26.

The spectrogram at fig. 5.27 shows both of the secondary peaks, and we can clearly see that the one at higher frequencies is bigger. We can also note that the main peak is still strong after 23 milliseconds, while the secondary peaks only last for around 4.

Last we have our type III merger from the simulation H4-q10-M1200. Once again we have $q = 1$ and so we use Equations (4.4) to (4.6). This is a typical type III postmerger spectrum as we can see at Figures 5.28 and 5.29. The f_{2-0} is not completely absent as there is a small peak at around 940 Hz where we should expect it based on our equations. However it is the inspiral secondary peak which is clearly bigger. The difference becomes even more apparent at the logarithmic scale.

The accuracy of our lines is once again great, helping as distinguish between

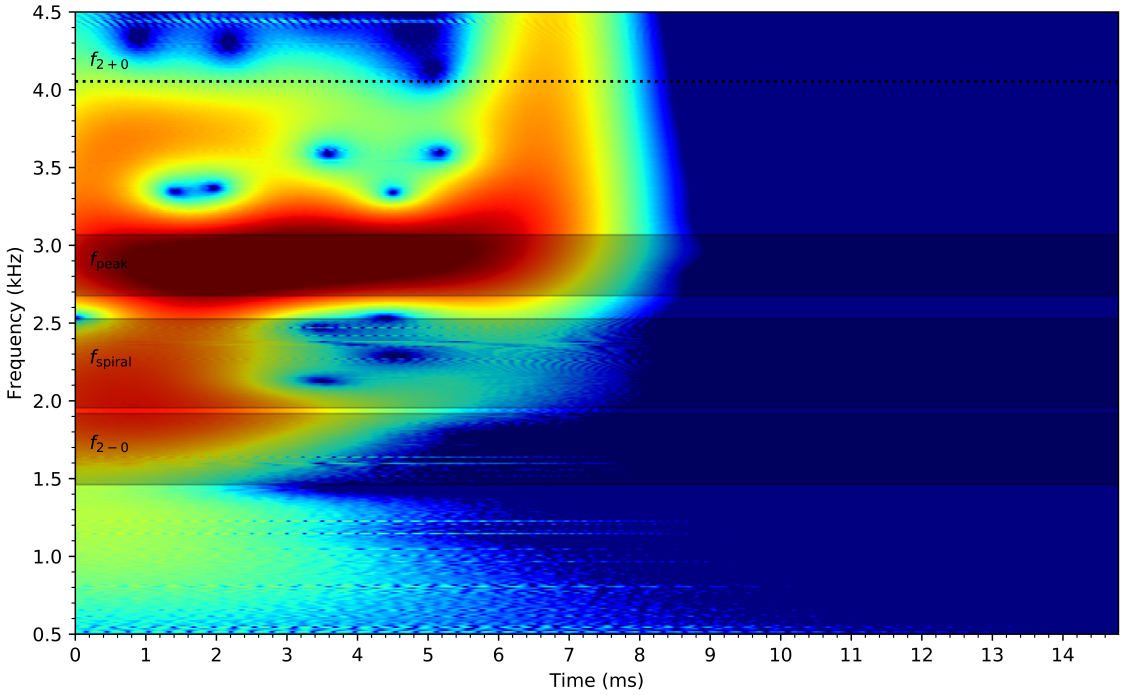

Figure 5.24: The spectrogram of ALF2-q10-M1400. We can see the main peak and also the two secondary peaks above and below 2 kHz. Also one high frequency peak.

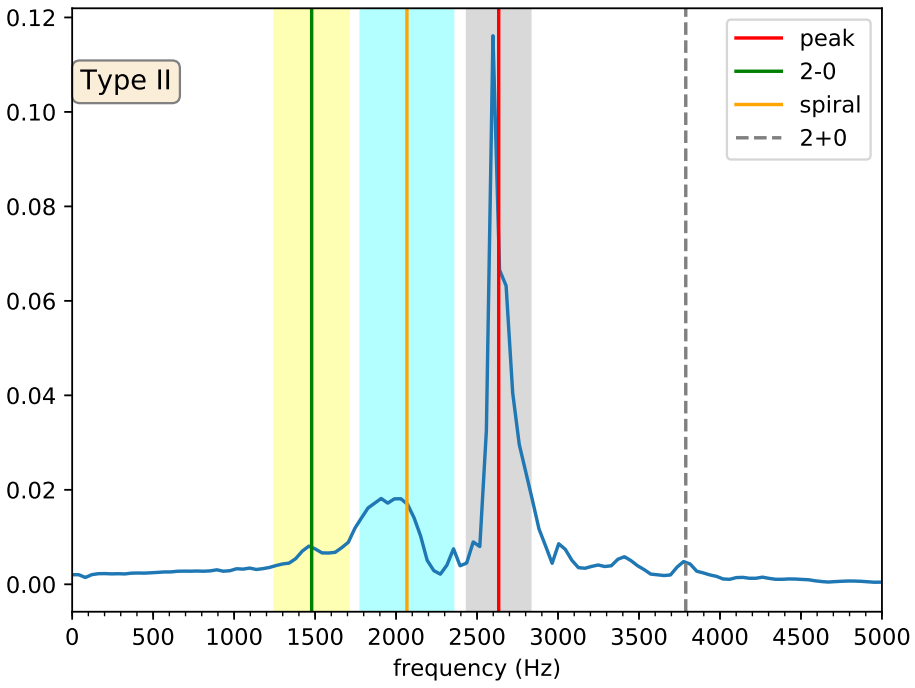

Figure 5.25: The linear frequency plot for ALF2-q10-M1300. We can see that the inspiral and (2-0) frequency amplitudes are almost at the same level.

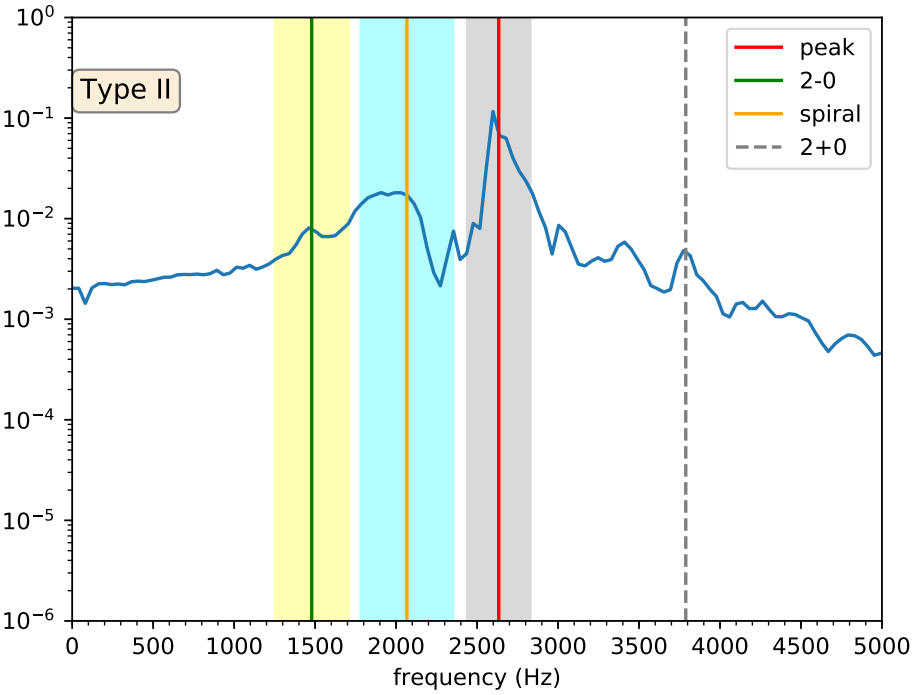

Figure 5.26: The frequency spectrum for ALF2-q10-M1300 in logarithmic scale.

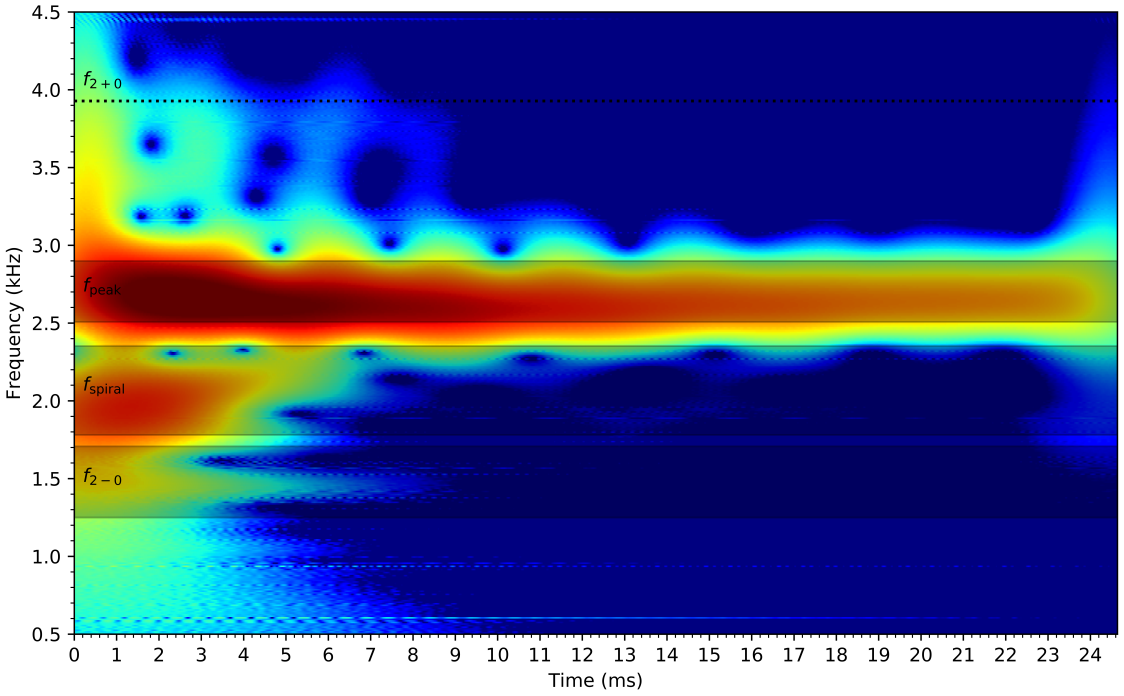

Figure 5.27: The spectrogram of ALF2-q10-M1300. We can see the main peak ,the two distinguished secondary peaks and also a small high-frequency secondary peak.

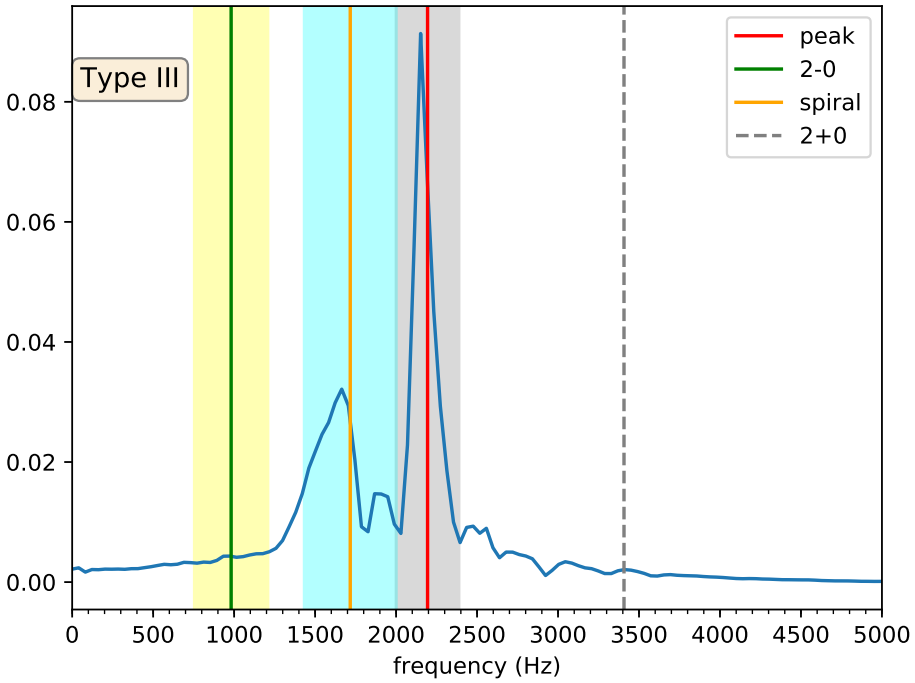

Figure 5.28: The linear frequency plot for H4-q10-M1200. It is a type III binary neutron star merger as we can see from the dominant secondary peak which is the inspiral $f_{\rm spiral}$.

the different peaks. On the log scale we can see that we can accurately predict the (2+0) peak, even if it is not so apparent, especially on a linear scale.

The spectrogram fig. 5.30 shows only one secondary peak, which from our previous discussion is the $f_{\rm spiral}$. We can see how it affects only the early postmerger stages and has no affect at the later stages.

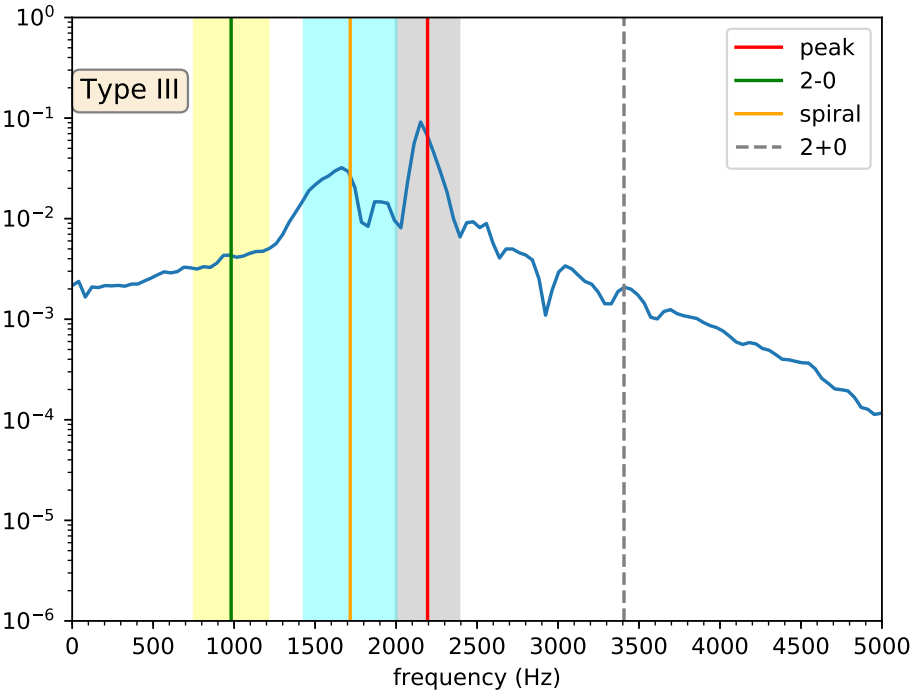

Figure 5.29: A logarithmic view of the H4-q10-M1200 frequency spectrum.

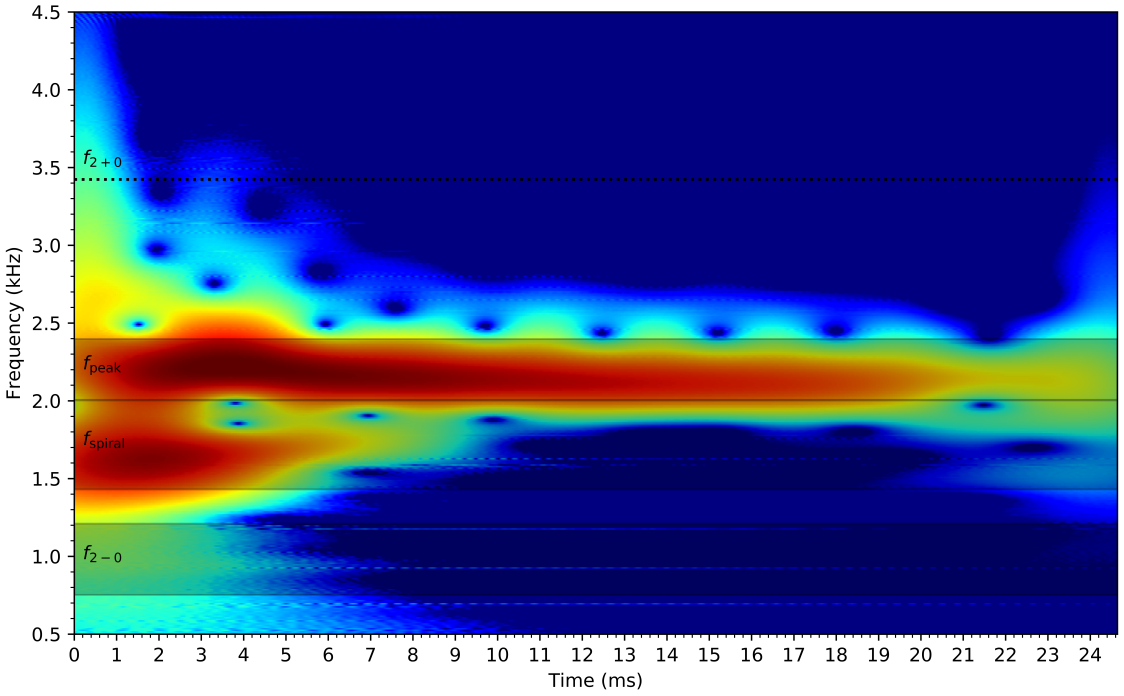

Figure 5.30: The spectrogram of H4-q10-M1200. There are two obvious peaks, one is the dominant main peak and the second is the inspiral secondary peak.

Appendix A

EOS

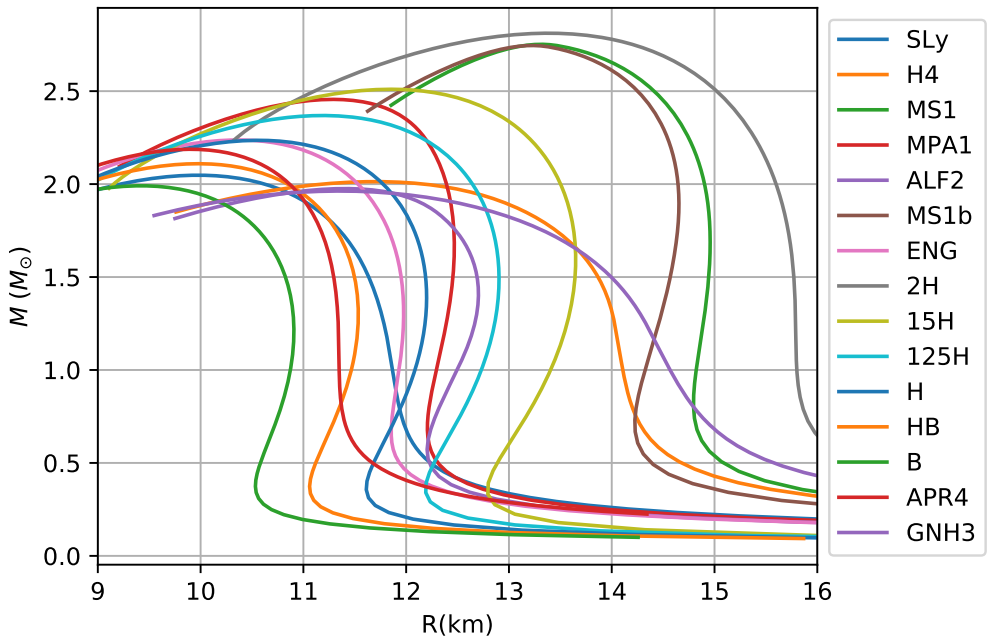

Figure A.1: The $M(R)$ figure for all the EOS that were used during this thesis.

Table A.1: The characteristic radii for masses $1.6M_\odot$ and $1.8M_\odot$ used in Equations (4.1) to (4.6) for every EOS used in this thesis.

EOS	$R_{1.6}$(km)	$R_{1.8}$(km)	EOS	$R_{1.6}$(km)	$R_{1.8}$(km)
SLy	11.55	11.27	15H	13.65	13.61
H4	13.74	13.32	125H	12.89	12.82
MS1	14.95	14.95	H	12.16	12.04
MPA1	12.47	12.46	HB	11.45	11.26
ALF2	12.64	12.40	B	10.75	10.47
MS1b	14.60	14.65	APR4	11.26	11.13
ENG	11.92	11.79	GNH3	13.79	13.12
2H	15.76	15.70			

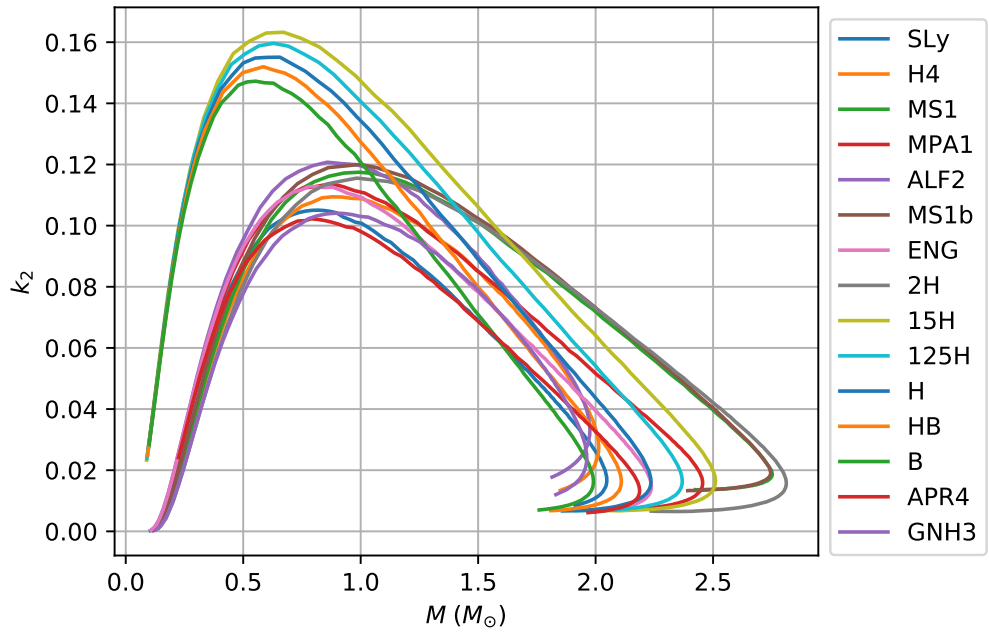

Figure A.2: The love number as a relation of mass for all the EOS that were used during this thesis. You can see the discussion at chapter 2.

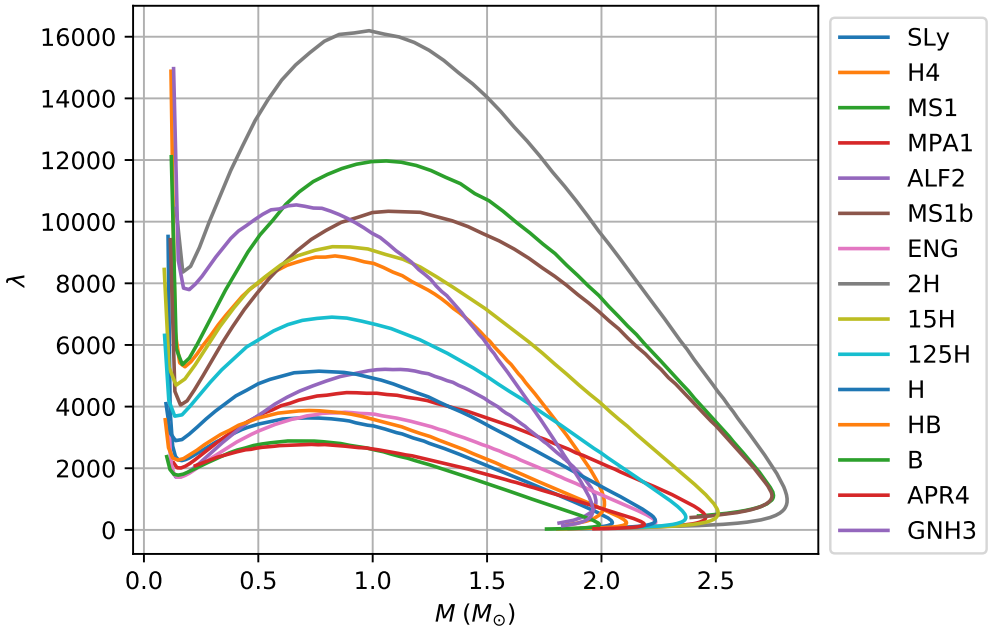

Figure A.3: The dimensionless tidal deformability as a relation of mass for all the EOS that were used during this thesis. More information about this type of figures at chapter 2.

Appendix B

CoRe

You can find the $M(R)$ diagram containing the whole dataset used for this thesis at fig. 4.1

The results of the whole dataset should be available here `https://github.com/johnkou97/postmerger_frequencies/tree/master/results`. You can also use the scripts which are available at `https://github.com/johnkou97/postmerger_frequencies` in order to reproduce the results or test anything you might want

Table B.1: The data for all the CoRe simulations. From left to right we have the ID number (from the BAM CoRe catalog), the EOS, the total mass of the system in solar masses, the mass ratio of the binary, the chirp Mass of the system, the main and secondary peaks frequency as expected from [28] in kHz and if the mass ratio is 1 we have the frequencies from Equations (4.1) to (4.3). The last collumn shows the type of the merger as discussed in chapter 4.

ID #	EOS	Mass	q	$M_{\rm chirp}$	$f_{\rm peak}$	$f_{\rm spir}$	f_{2-0}	$f_{\rm peak}^{q=1}$	$f_{\rm spir}^{q=1}$	$f_{2-0}^{q=1}$	Type
002	2H	2.70	1.00	1.18	1.99	1.35	0.94	2.01	1.50	0.91	3
003	ALF2	2.70	1.00	1.18	2.81	2.11	1.56	2.79	2.15	1.58	1
004	ALF2	2.70	1.00	1.18	2.81	2.11	1.57	2.79	2.15	1.59	1
009	ALF2	2.50	1.27	1.08	2.62	1.93	1.34	-	-	-	2
010	ALF2	2.70	1.16	1.17	2.80	2.11	1.56	-	-	-	1
022	ENG	2.70	1.00	1.18	3.06	2.33	1.89	3.11	2.36	1.90	1
035	H4	2.70	1.00	1.18	2.48	1.83	1.20	2.40	1.89	1.22	3
036	H4	2.70	1.00	1.18	2.48	1.83	1.20	2.40	1.89	1.22	3
046	H4	2.70	1.16	1.17	2.48	1.83	1.19	-	-	-	3
048	H4	2.75	1.25	1.19	2.50	1.85	1.22	-	-	-	2
053	H4	2.75	1.50	1.17	2.47	1.82	1.19	-	-	-	2
057	H4	2.75	1.75	1.14	2.43	1.79	1.14	-	-	-	2
058	MPA1	2.70	1.00	1.18	2.78	2.09	1.64	2.86	2.13	1.65	1
059	MS1	2.70	1.16	1.17	2.09	1.46	0.97	-	-	-	3
061	MS1	2.70	1.00	1.18	2.09	1.47	0.98	2.12	1.58	0.98	3
065	MS1b	2.70	1.00	1.18	2.15	1.52	1.02	2.18	1.63	1.03	3

Continued on next page

Table B.1 – *Continued from previous page*

ID #	EOS	Mass	q	$M_{\rm chirp}$	$f_{\rm peak}$	$f_{\rm spir}$	f_{2-0}	$f_{\rm peak}^{q=1}$	$f_{\rm spir}^{q=1}$	$f_{2-0}^{q=1}$	Type
070	MS1b	2.75	1.00	1.20	2.17	1.54	1.05	2.21	1.64	1.07	3
080	MS1b	2.50	1.27	1.08	2.06	1.46	0.90	-	-	-	3
089	MS1b	2.75	1.25	1.19	2.16	1.53	1.04	-	-	-	3
090	MS1b	3.20	1.00	1.39	2.39	1.71	1.33	2.46	1.82	1.37	2
091	MS1b	2.75	1.50	1.17	2.14	1.52	1.01	-	-	-	3
092	MS1b	3.40	1.00	1.48	2.52	1.82	1.47	2.58	1.92	1.51	2
093	MS1b	2.75	1.75	1.14	2.12	1.50	0.98	-	-	-	3
098	SLy	2.70	1.00	1.18	3.30	2.53	2.08	3.30	2.55	2.08	1
107	SLy	2.46	1.22	1.06	3.01	2.24	1.75	-	-	-	1
121	SLy	2.50	1.27	1.08	3.05	2.27	1.79	-	-	-	1
122	SLy	2.60	1.17	1.13	3.17	2.40	1.94	-	-	-	1
123	SLy	2.70	1.16	1.17	3.29	2.52	2.07	-	-	-	1
124	SLy	2.50	1.50	1.06	3.00	2.23	1.74	-	-	-	1
126	SLy	2.75	1.25	1.19	3.34	2.56	2.13	-	-	-	1
128	SLy	2.75	1.50	1.17	3.28	2.50	2.06	-	-	-	1

Appendix C

Sacra

The results of the whole dataset should be available here `https://github.com/johnkou97/sacra/tree/master/results`. You can also use the scripts which are available at `https://github.com/johnkou97/sacra` in order to reproduce the results or test anything you might want

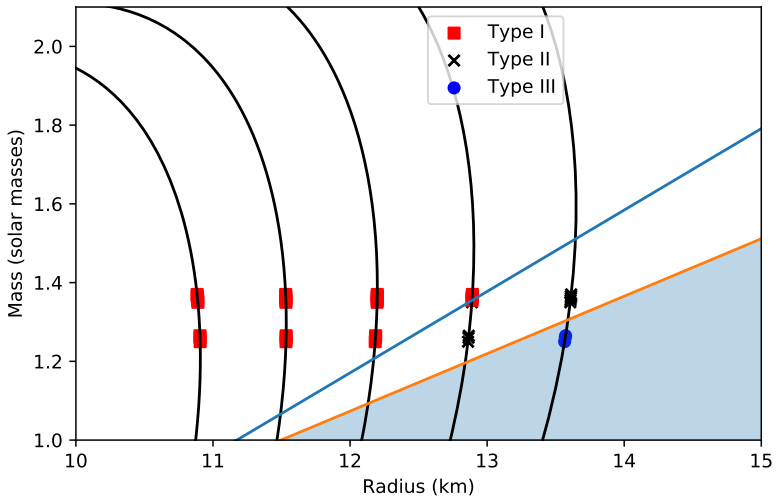

Figure C.1: The $M(R)$ diagram for every simulation from the Sacra Catalog. It also shows the type of the merger as explained in chapter 4.

Table C.1: The values of the density at the turning point of each EOS for the Sacra Catalog. Each density is what defines every EOS.

EOS	ρ [g cm^{-3}]
15H	9.3108×10^{13}
125H	1.0711×10^{14}
H	1.2323×10^{14}
HB	1.4177×10^{14}
B	1.6309×10^{14}

Table C.2: The data for all the Sacra simulations. From left to right we have the EOS, the total mass of the system in solar masses, the mass ratio of the binary, the main and secondary peaks frequency as expected from [28] in kHz and if the mass ratio is 1 we have the frequencies from Equations (4.1) to (4.3). We have also the (2+0) frequency from eq. (5.1). The last column shows the type of the merger as discussed in chapter 4.

EOS	Mass	q	$M_{\rm chirp}$	$f_{\rm peak}$	$f_{\rm spir}$	f_{2-0}	f_{2+0}	$f_{\rm peak}^{q=1}$	$f_{\rm spir}^{q=1}$	$f_{2-0}^{q=1}$	$f_{2+0}^{q=1}$	Type
15H	2.70	1.00	1.18	2.40	1.76	1.22	3.57	2.43	1.82	1.25	3.61	2
15H	2.71	1.17	1.18	2.40	1.76	1.22	3.57	-	-	-	-	2
15H	2.50	1.00	1.09	2.28	1.65	1.07	3.49	2.29	1.72	1.08	3.50	3
15H	2.72	1.25	1.18	2.40	1.76	1.22	3.57	-	-	-	-	2
15H	2.73	1.31	1.18	2.40	1.76	1.22	3.57	-	-	-	-	2
15H	2.73	1.33	1.17	2.40	1.75	1.22	3.57	-	-	-	-	2
15H	2.74	1.36	1.18	2.40	1.76	1.22	3.57	-	-	-	-	2
15H	2.52	1.25	1.09	2.28	1.65	1.07	3.49	-	-	-	-	3
15H	2.53	1.36	1.09	2.28	1.65	1.07	3.48	-	-	-	-	3
125H	2.70	1.00	1.18	2.65	1.98	1.47	3.84	2.69	2.03	1.49	3.89	2
125H	2.71	1.17	1.18	2.65	1.98	1.47	3.84	-	-	-	-	1
125H	2.50	1.00	1.09	2.50	1.84	1.28	3.72	2.53	1.88	1.29	3.77	2
125H	2.72	1.25	1.18	2.65	1.98	1.47	3.84	-	-	-	-	1
125H	2.73	1.31	1.18	2.65	1.98	1.47	3.84	-	-	-	-	1
125H	2.73	1.33	1.17	2.65	1.98	1.46	3.83	-	-	-	-	1
125H	2.74	1.36	1.18	2.65	1.98	1.47	3.84	-	-	-	-	1
125H	2.52	1.25	1.09	2.50	1.84	1.28	3.72	-	-	-	-	2
125H	2.53	1.36	1.09	2.49	1.83	1.27	3.72	-	-	-	-	2
H	2.70	1.00	1.18	2.95	2.24	1.77	4.13	3.00	2.27	1.78	4.21	1
H	2.71	1.17	1.18	2.95	2.24	1.77	4.13	-	-	-	-	1
H	2.50	1.00	1.09	2.76	2.05	1.55	3.98	2.81	2.08	1.55	4.07	1
H	2.72	1.25	1.18	2.95	2.24	1.77	4.13	-	-	-	-	1
H	2.73	1.31	1.18	2.95	2.24	1.77	4.13	-	-	-	-	1
H	2.73	1.33	1.17	2.95	2.23	1.77	4.13	-	-	-	-	1
H	2.74	1.36	1.18	2.95	2.24	1.77	4.13	-	-	-	-	1
H	2.52	1.25	1.09	2.76	2.05	1.55	3.98	-	-	-	-	1
H	2.53	1.36	1.09	2.76	2.04	1.54	3.98	-	-	-	-	1
HB	2.70	1.00	1.18	3.30	2.53	2.14	4.47	3.35	2.55	2.13	4.57	1
HB	2.71	1.17	1.18	3.30	2.53	2.14	4.47	-	-	-	-	1
HB	2.50	1.00	1.09	3.07	2.30	1.87	4.28	3.13	2.32	1.86	4.40	1
HB	2.72	1.25	1.18	3.30	2.53	2.14	4.47	-	-	-	-	1
HB	2.73	1.31	1.18	3.30	2.53	2.14	4.47	-	-	-	-	1
HB	2.73	1.33	1.17	3.30	2.52	2.13	4.47	-	-	-	-	1
HB	2.74	1.36	1.18	3.31	2.53	2.14	4.47	-	-	-	-	1
HB	2.52	1.25	1.09	3.08	2.30	1.87	4.28	-	-	-	-	1
HB	2.53	1.36	1.09	3.07	2.29	1.86	4.28	-	-	-	-	1
B	2.70	1.00	1.18	3.71	2.86	2.56	4.87	3.75	2.89	2.52	4.97	1

Continued on next page

Table C.2 – *Continued from previous page*

EOS	Mass	q	$M_{\rm chirp}$	$f_{\rm peak}$	$f_{\rm spir}$	f_{2-0}	f_{2+0}	$f_{\rm peak}^{q=1}$	$f_{\rm spir}^{q=1}$	$f_{2-0}^{q=1}$	$f_{2+0}^{q=1}$	Type
B	2.71	1.17	1.18	3.71	2.86	2.56	4.87	-	-	-	-	1
B	2.50	1.00	1.09	3.44	2.58	2.24	4.64	3.50	2.61	2.21	4.78	1
B	2.72	1.25	1.18	3.71	2.86	2.56	4.87	-	-	-	-	1
B	2.73	1.31	1.18	3.71	2.86	2.56	4.87	-	-	-	-	1
B	2.73	1.33	1.17	3.71	2.86	2.55	4.86	-	-	-	-	1
B	2.74	1.36	1.18	3.71	2.87	2.56	4.87	-	-	-	-	1
B	2.52	1.25	1.09	3.44	2.59	2.24	4.64	-	-	-	-	1
B	2.53	1.36	1.09	3.43	2.58	2.23	4.63	-	-	-	-	1

Appendix D

Takami and Rezzolla

The results of the whole dataset should be available here `https://github.com/johnkou97/takami/tree/master/results`. You can also use the scripts which are available at `https://github.com/johnkou97/takami` in order to reproduce the results or test anything you might want

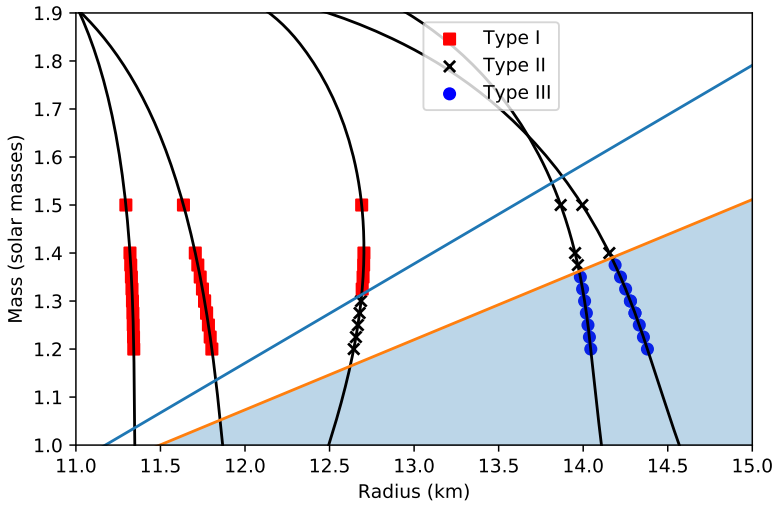

Figure D.1: The $M(R)$ diagram for every simulation from the Takami and Rezzolla Catalog. It also shows the type of the merger as explained in chapter 4.

Table D.1: The data for all the Takami and Rezzolla Catalog simulations. From left to right we have the EOS, the total mass of the system in solar masses, the mass ratio of the binary, the main and secondary peaks frequency as expected from [28] in kHz and if the mass ratio is 1 we have the frequencies from Equations (4.1) to (4.3). We have also the (2+0) frequency from eq. (5.1). The last column shows the type of the merger as discussed in chapter 4.

EOS	Mass	q	$M_{\rm chirp}$	$f_{\rm peak}$	$f_{\rm spir}$	f_{2-0}	f_{2+0}	$f_{\rm peak}^{q=1}$	$f_{\rm spir}^{q=1}$	$f_{2-0}^{q=1}$	$f_{2+0}^{q=1}$	Type
ALF2	2.40	1.00	1.04	2.55	1.87	1.27	3.84	2.54	1.91	1.28	3.80	2.00
ALF2	2.45	1.00	1.07	2.59	1.91	1.32	3.87	2.58	1.95	1.33	3.83	2.00
ALF2	2.50	1.00	1.09	2.64	1.95	1.36	3.91	2.62	1.99	1.38	3.86	2.00
ALF2	2.55	1.00	1.11	2.68	1.99	1.41	3.94	2.66	2.03	1.43	3.90	2.00
ALF2	2.60	1.00	1.13	2.72	2.03	1.46	3.98	2.70	2.07	1.48	3.93	2.00
ALF2	2.65	1.00	1.15	2.76	2.07	1.51	4.01	2.75	2.11	1.53	3.96	1.00
ALF2	2.70	1.00	1.18	2.81	2.11	1.56	4.05	2.79	2.15	1.58	3.99	1.00
ALF2	2.75	1.00	1.20	2.85	2.16	1.62	4.09	2.83	2.20	1.64	4.02	1.00
ALF2	2.80	1.00	1.22	2.90	2.20	1.67	4.13	2.87	2.24	1.69	4.05	1.00
ALF2	3.00	1.00	1.31	3.09	2.40	1.89	4.30	3.04	2.44	1.91	4.18	1.00
APR4	2.40	1.00	1.04	3.02	2.23	1.82	4.21	3.11	2.26	1.82	4.41	1.00
APR4	2.45	1.00	1.07	3.07	2.29	1.89	4.26	3.17	2.31	1.88	4.46	1.00
APR4	2.50	1.00	1.09	3.13	2.34	1.96	4.30	3.23	2.37	1.95	4.50	1.00
APR4	2.55	1.00	1.11	3.19	2.40	2.03	4.35	3.28	2.43	2.02	4.54	1.00
APR4	2.60	1.00	1.13	3.25	2.46	2.10	4.39	3.34	2.48	2.09	4.59	1.00
APR4	2.65	1.00	1.15	3.31	2.52	2.17	4.44	3.40	2.54	2.16	4.63	1.00
APR4	2.70	1.00	1.18	3.37	2.58	2.25	4.49	3.45	2.61	2.23	4.67	1.00
APR4	2.75	1.00	1.20	3.43	2.65	2.32	4.54	3.51	2.67	2.30	4.72	1.00
APR4	2.80	1.00	1.22	3.49	2.71	2.40	4.59	3.57	2.73	2.37	4.76	1.00
APR4	3.00	1.00	1.31	3.76	2.99	2.71	4.81	3.80	3.01	2.67	4.93	1.00
GNH3	2.40	1.00	1.04	2.34	1.70	0.97	3.72	2.19	1.76	0.97	3.41	3.00
GNH3	2.45	1.00	1.07	2.38	1.73	1.01	3.75	2.22	1.78	1.01	3.44	3.00
GNH3	2.50	1.00	1.09	2.41	1.76	1.04	3.78	2.26	1.82	1.05	3.46	3.00
GNH3	2.55	1.00	1.11	2.44	1.79	1.08	3.81	2.29	1.85	1.09	3.49	3.00
GNH3	2.60	1.00	1.13	2.48	1.82	1.11	3.84	2.32	1.88	1.13	3.51	3.00
GNH3	2.65	1.00	1.15	2.51	1.86	1.15	3.88	2.35	1.91	1.17	3.54	3.00
GNH3	2.70	1.00	1.18	2.55	1.89	1.19	3.91	2.39	1.94	1.21	3.56	3.00
GNH3	2.75	1.00	1.20	2.59	1.92	1.23	3.95	2.42	1.98	1.25	3.59	3.00
GNH3	2.80	1.00	1.22	2.62	1.96	1.26	3.98	2.45	2.01	1.29	3.61	2.00
GNH3	3.00	1.00	1.31	2.78	2.12	1.42	4.14	2.58	2.17	1.46	3.71	2.00
GNH3	2.55	0.82	1.10	2.43	1.78	1.07	3.80	-	-	-	-	3.00
GNH3	2.60	1.08	1.13	2.48	1.82	1.11	3.84	-	-	-	-	3.00
H4	2.40	1.00	1.04	2.29	1.66	0.98	3.60	2.20	1.72	0.98	3.42	3.00
H4	2.45	1.00	1.07	2.32	1.69	1.02	3.63	2.24	1.74	1.02	3.45	3.00
H4	2.50	1.00	1.09	2.35	1.71	1.05	3.66	2.27	1.77	1.06	3.48	3.00
H4	2.55	1.00	1.11	2.39	1.74	1.09	3.68	2.30	1.80	1.10	3.50	3.00

Continued on next page

Table D.1 – *Continued from previous page*

EOS	Mass	q	$M_{\rm chirp}$	$f_{\rm peak}$	$f_{\rm spir}$	f_{2-0}	f_{2+0}	$f_{\rm peak}^{q=1}$	$f_{\rm spir}^{q=1}$	$f_{2-0}^{q=1}$	$f_{2+0}^{q=1}$	Type
H4	2.60	1.00	1.13	2.42	1.77	1.12	3.71	2.33	1.83	1.14	3.53	3.00
H4	2.65	1.00	1.15	2.45	1.80	1.16	3.74	2.37	1.86	1.18	3.55	3.00
H4	2.70	1.00	1.18	2.48	1.83	1.20	3.77	2.40	1.89	1.22	3.58	3.00
H4	2.75	1.00	1.20	2.52	1.86	1.24	3.80	2.43	1.92	1.26	3.60	2.00
H4	2.80	1.00	1.22	2.55	1.90	1.28	3.83	2.46	1.96	1.30	3.63	2.00
H4	3.00	1.00	1.31	2.70	2.04	1.44	3.97	2.60	2.10	1.47	3.73	2.00
SLy	2.40	1.00	1.04	2.96	2.19	1.69	4.23	2.98	2.22	1.69	4.27	1.00
SLy	2.45	1.00	1.07	3.02	2.24	1.75	4.28	3.03	2.27	1.75	4.31	1.00
SLy	2.50	1.00	1.09	3.07	2.30	1.82	4.33	3.09	2.32	1.82	4.35	1.00
SLy	2.55	1.00	1.11	3.13	2.35	1.88	4.37	3.14	2.38	1.88	4.40	1.00
SLy	2.60	1.00	1.13	3.18	2.41	1.95	4.42	3.19	2.43	1.95	4.44	1.00
SLy	2.65	1.00	1.15	3.24	2.47	2.02	4.47	3.24	2.49	2.01	4.48	1.00
SLy	2.70	1.00	1.18	3.30	2.53	2.08	4.52	3.30	2.55	2.08	4.52	1.00
SLy	2.75	1.00	1.20	3.36	2.59	2.15	4.57	3.35	2.61	2.15	4.56	1.00
SLy	2.80	1.00	1.22	3.42	2.65	2.22	4.62	3.41	2.67	2.21	4.60	1.00
SLy	3.00	1.00	1.31	3.68	2.92	2.52	4.84	3.62	2.94	2.49	4.76	1.00
SLy	2.55	0.82	1.10	3.11	2.34	1.86	4.36	-	-	-	-	1.00
SLy	2.60	1.08	1.13	3.18	2.41	1.95	4.42	-	-	-	-	1.00

Bibliography

[1]J. A. Faber and F. A. Rasio, "Binary neutron star mergers", Living Reviews in Relativity **15**, 10.12942/lrr-2012-8 (2012).

[2]M. Maggiore, *Gravitational Waves. Vol. 1: Theory and Experiments*, Oxford Master Series in Physics (Oxford University Press, 2007).

[3]D. G. Blair, *The Detection of Gravitational Waves* (2005).

[4]M. Pitkin, S. Reid, S. Rowan, and J. Hough, "Gravitational Wave Detection by Interferometry (Ground and Space)", Living Reviews in Relativity **14**, 5, 5 (2011).

[5]B. S. Sathyaprakash and B. F. Schutz, "Physics, Astrophysics and Cosmology with Gravitational Waves", Living Reviews in Relativity **12**, 2, 2 (2009).

[6]K. S. Thorne, "Black holes and time warps. Einstein's outrageous legacy. Chapter 9: Serendipity.", Priroda **11**, 87–105 (1994).

[7]A. Hewish, S. J. Bell, J. D. H. Pilkington, P. F. Scott, and R. A. Collins, "Observation of a Rapidly Pulsating Radio Source", Nature **217**, 709–713 (1968).

[8]R. A. Hulse and J. H. Taylor, "Discovery of a pulsar in a binary system.", Astrophysical Journal, Letters **195**, L51–L53 (1975).

[9]C. I. of Technology, *Ligo home page*, https://www.ligo.caltech.edu/.

[10]B. C. Barish, "Ligo: Status and Prospects", in New worlds in astroparticle physics, edited by A. M. Mourao, M. Pimenta, R. Potting, and P. Sonderegger (Jan. 1998), p. 391.

[11]INFN, *Virgo home page*, https://www.virgo-gw.eu/.

[12]A. Brillet and Virgo Collaboration, "VIRGO - Status Report, November 1997", in Second edoardo amaldi conference on gravitational wave experiments, edited by E. Coccia, G. Veneziano, and G. Pizzella (Jan. 1998), p. 86.

[13]U. of Hanover, *Geo600 home page*, https://www.geo600.org/.

[14]J. Hough, G. P. Newton, N. A. Robertson, H. Ward, M. Plissi, D. Robertson, S. Rowan, K. D. Skeldon, K. A. Strain, M. Casey, P. McNamara, C. Torrie, S. Twyford, K. Danzmann, H. Lück, M. Schrempel, B. Willke, P. Aufmuth, S. Brozek, A. Rüdiger, R. Schilling, W. Winkler, G. Heinzel, J. Mizuno, D. Schnier, and B. F. Schutz, "GEO 600: Current Status and Some Aspects of the Design", in Gravitational wave detection, edited by K. Tsubono, M. .-. Fujimoto, and K. Kuroda (Jan. 1997), p. 175.

[15]T. National Astronomy Observatory, *Tama home page*, http://gwpo.nao.ac.jp/en/.

[16]K. Tsubono and TAMA Collaboration, "TAMA Project", in Gravitational wave detection, edited by K. Tsubono, M. .-. Fujimoto, and K. Kuroda (Jan. 1997), p. 183.

[17]J. R. Oppenheimer and G. M. Volkoff, "On Massive Neutron Cores", Physical Review **55**, 374–381 (1939).

[18]J. S. Read, C. Markakis, M. Shibata, K. Uryū, J. D. E. Creighton, and J. L. Friedman, "Measuring the neutron star equation of state with gravitational wave observations", Physical Review D **79**, 124033, 124033 (2009).

[19]J. S. Read, B. D. Lackey, B. J. Owen, and J. L. Friedman, "Constraints on a phenomenologically parametrized neutron-star equation of state", Physical Review D **79**, 124032, 124032 (2009).

[20]T. Hinderer, B. D. Lackey, R. N. Lang, and J. S. Read, "Tidal deformability of neutron stars with realistic equations of state and their gravitational wave signatures in binary inspiral", Physical Review D **81**, 123016, 123016 (2010).

[21]N. Stergioulas, *Niksterg/pytovpp*, `https://github.com/niksterg/pyTOVpp`.

[22]I. Koutalios, *Johnkou97/pytovpp*, `https://github.com/johnkou97/pyTOVpp`.

[23]T. Hinderer, "Tidal Love Numbers of Neutron Stars", Astrophysical Journal **677**, 1216–1220 (2008).

[24]A. Guerra Chaves and T. Hinderer, "Probing the equation of state of neutron star matter with gravitational waves from binary inspirals in light of GW170817: a brief review", Journal of Physics G Nuclear Physics **46**, 123002, 123002 (2019).

[25]T. Dietrich, D. Radice, S. Bernuzzi, F. Zappa, A. Perego, B. Brügmann, S. Vivekanandji Chaurasia, R. Dudi, W. Tichy, and M. Ujevic, "CoRe database of binary neutron star merger waveforms", Classical and Quantum Gravity **35**, 24LT01, 24LT01 (2018).

[26]N. Stergioulas, A. Bauswein, K. Zagkouris, and H.-T. Janka, "Gravitational waves and non-axisymmetric oscillation modes in mergers of compact object binaries", Monthly Notices of the RAS **418**, 427–436 (2011).

[27]A. Bauswein and N. Stergioulas, "Unified picture of the post-merger dynamics and gravitational wave emission in neutron star mergers", Physical Review D **91**, 124056, 124056 (2015).

[28]S. Vretinaris, N. Stergioulas, and A. Bauswein, "Empirical relations for gravitational-wave asteroseismology of binary neutron star mergers", Physical Review D **101**, 084039, 084039 (2020).

[29]K. Kiuchi, K. Kawaguchi, K. Kyutoku, Y. Sekiguchi, M. Shibata, and K. Taniguchi, "Sub-radian-accuracy gravitational waveforms of coalescing binary neutron stars in numerical relativity", Physical Review D **96**, 084060, 084060 (2017).

[30]K. Kiuchi, K. Kawaguchi, K. Kyutoku, Y. Sekiguchi, and M. Shibata, "Sub-radian-accuracy gravitational waves from coalescing binary neutron stars in numerical relativity. II. Systematic study on the equation of state, binary mass, and mass ratio", Physical Review D **101**, 084006, 084006 (2020).

[31]L. Rezzolla and K. Takami, "Gravitational-wave signal from binary neutron stars: A systematic analysis of the spectral properties", Physical Review D **93**, 124051, 124051 (2016).